JACS
JOURNAL OF THE AMERICAN CHEMICAL SOCIETY
pubs.acs.org/JACS
Article

Immobilization of the Polar Group into an Ultramicroporous Metal−Organic Framework Enabling Benchmark Inverse Selective CO_2/C_2H_2 Separation with Record C_2H_2 Production

Shan-Qing Yang, Rajamani Krishna, Hongwei Chen, Libo Li, Lei Zhou, Yi-Feng An, Fei-Yang Zhang, Qiang Zhang, Ying-Hui Zhang, Wei Li, Tong-Liang Hu,* and Xian-He Bu

Cite This: J. Am. Chem. Soc. 2023, 145, 13901−13911

Read Online

ACCESS | Metrics & More | Article Recommendations | Supporting Information

ABSTRACT: One-step harvest of high-purity light hydrocarbons without the desorption process represents an advanced and highly efficient strategy for the purification of target substances. The separation and purification of acetylene (C_2H_2) from carbon dioxide (CO_2) by CO_2-selective adsorbents are urgently demanded yet are very challenging owing to their similar physicochemical properties. Here, we employ the pore chemistry strategy to adjust the pore environment by immobilizing polar groups into an ultramicroporous metal−organic framework (MOF), achieving one-step manufacture of high-purity C_2H_2 from CO_2/C_2H_2 mixtures. Embedding methyl groups into prototype stable MOF (Zn-ox-trz) not only changes the pore environment but also improves the discrimination of guest molecules. The methyl-functionalized **Zn-ox-mtz** thus exhibits the benchmark reverse CO_2/C_2H_2 uptake ratio of 12.6 (123.32/9.79 cm^3 cm^{-3}) and an exceptionally high equimolar CO_2/C_2H_2 selectivity of 1064.9 at ambient conditions. Molecular simulations reveal that the synergetic effect of pore confinement and surfaces decorated with methyl groups provides high recognition of CO_2 molecules through multiple van der Waals interactions. The column breakthrough experiments suggest that **Zn-ox-mtz** dramatically achieved the one-step purification capacity of C_2H_2 from the CO_2/C_2H_2 mixture with a record C_2H_2 productivity of 2091 mmol kg^{-1}, surpassing all of the CO_2-selective adsorbents reported so far. In addition, **Zn-ox-mtz** exhibits excellent chemical stability under different pH values of aqueous solutions (pH = 1−12). Moreover, the highly stable framework and excellent inverse selective CO_2/C_2H_2 separation performance showcase its promising application as a C_2H_2 splitter for industrial manufacture. This work paves the way to developing reverse-selective adsorbents for the challenging gas separation process.

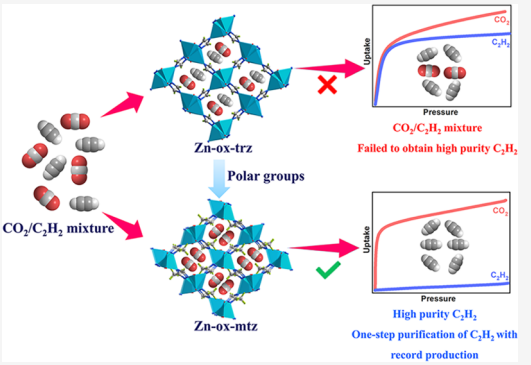

INTRODUCTION

The separation and purification of gaseous mixtures are particularly important in the petrochemical industry to produce high-value downstream chemicals such as fuel, plastics, and polymers.[1,2] Acetylene (C_2H_2), as the simplest alkyne, is not only a vital gas fuel but also an important precursor chemical and basic building block in the industry, which is generally used to produce high-value chemicals such as acrylic acid, 1,4-butynediol, and 1,4-butynediol.[3] C_2H_2 is generally derived from the steam cracking of petroleum or/and naphtha and methane partial combustion, in this context, carbon dioxide (CO_2) contaminant inevitably draws into the product of crude C_2H_2.[4] Therefore, the removal of CO_2 impurity is a necessary step before further manufacturing high-value-added chemicals. CO_2 and C_2H_2 molecules exhibit highly similar physical properties and possess close molecular shapes and sizes, such as boiling point (C_2H_2: 189.3 K and CO_2: 194.7 K) and molecular size (C_2H_2: 3.34 × 3.32 × 5.70 $Å^3$ and CO_2: 3.33 × 3.18 × 5.36 $Å^3$) (Scheme 1).[5] In addition, both CO_2 and C_2H_2 are nonpolar linear molecules with almost identical kinetic diameters of approximately 3.3 Å. Given their similar physical properties, there is no doubt that the

Scheme 1. Comparison of the Molecular Structure and Physical Property of CO_2 (Left) and C_2H_2 (Right)

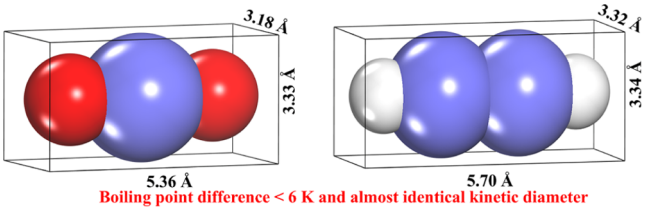

Received: March 29, 2023
Published: June 13, 2023

https://doi.org/10.1021/jacs.3c03265
J. Am. Chem. Soc. 2023, 145, 13901−13911

separation of the CO_2/C_2H_2 mixture is still a daunting challenging process,[6−9] in particular, removing the trace amounts of CO_2 from C_2H_2, and their separation has attracted the interest of scientists and engineers due to its scientific problem and industrial relevance. At present, the separation of the CO_2/C_2H_2 mixture mainly utilizes organic solvent extraction or/and cryogenic distillation,[4,10] which require high energy, are cost-intensive, and are environmentally unfriendly. Adsorptive separation using porous solid adsorbents based on the physical adsorption mechanism, such as pressure swing adsorption (PSA) and temperature swing adsorption (TSA), is an effective alternative technology, which is an economically viable and energy-efficient process and more environmentally friendly. Therefore, the development and design of novel porous adsorbents for the separation and purification of C_2H_2 from a CO_2/C_2H_2 mixture are urgently demanded yet challenging.

Extensive endeavors have been devoted to exploring porous solid adsorbents including but not limited to zeolites, activated carbons, metal−organic frameworks (MOFs), hydrogen-bonded organic frameworks (HOFs), covalent−organic frameworks (COFs), and hybrid ultramicroporous materials (HUMs).[11−16] Especially, MOFs, also called porous coordination polymers (PCPs), as novel porous organic−inorganic hybrid materials, are constructed from the self-assembly of metal ions or clusters and organic ligands, which become promising adsorbents for gas mixture separation owing to their tunable pore size and pore chemistry.[12,17,18] The rational design of the pore shape/size and pore chemistry based on the modular feature of MOFs in reticular chemistry and crystal engineering has enabled some MOF adsorbents to exhibit unprecedented adsorption and separation performance for hydrocarbons, including but not limited to C_2H_2/C_2H_4, C_2H_6/C_2H_4, and C_3H_6/C_3H_8.[19−23] However, the almost same kinetic diameter of CO_2 and C_2H_2 makes it greatly challenging for MOFs to differentiate these gases. Recently, a large number of MOF adsorbents have been reported to be used for CO_2/C_2H_2 separation, with almost all of them exhibiting a C_2H_2-selective adsorption behavior. The C_2H_2-selective MOFs could enhance the C_2H_2−framework interaction by designing interaction sites such as hydrogen-bonding interaction, Lewis basic interaction, and C_2H_2−metal π-complexation, obtaining C_2H_2/CO_2 separation ability.[24−29] However, such C_2H_2-selective MOF adsorbents need the desorption process to obtain high-purity C_2H_2; furthermore, the strong C_2H_2−framework interactions may cause more energy consumption in the desorption process. Given that the main impurity CO_2 accounts for 3−50% of the C_2H_2 crude,[11] the reverse CO_2-selective MOFs, i.e., preferential adsorption of CO_2 over C_2H_2, are more suitable for separation requirements. Compared with other complicated regeneration processes, it could save about 40% energy consumption by directly obtaining the product process.[30] Undoubtedly, the judicious design of reverse CO_2-selective MOFs is very important yet greatly difficult, and the reported CO_2-selective MOFs are still very rare.[9,18] With respect to practical industrial implementation processes, sufficient stability is a prerequisite for gas separation applications, especially the chemical stability tolerance of water, acids, and bases. Furthermore, the trade-off between reverse CO_2/C_2H_2 selectivity and CO_2 uptake is still a great obstacle in state-of-the-art adsorbents. For instance, the benchmark MOF Cu−F-pymo exhibits unprecedentedly high CO_2/C_2H_2 selectivity (>10^5), while the CO_2 uptake is only 26.6 $cm^3\ g^{-1}$, leading to low C_2H_2 productivity;[31] SIFSIX-3-Ni and CD-MOFs exhibit CO_2 adsorption uptakes of 98.4 and 60.4 $cm^3\ cm^{-3}$, while the reverse CO_2/C_2H_2 selectivities are only 7.7 and 6.6, respectively.[7,32] Thus, the construction of stable reverse CO_2-selective MOF adsorbents with high CO_2 uptake and high CO_2/C_2H_2 selectivity is a daunting challenge and yet important for the separation and purification of C_2H_2.

Since the kinetic diameters of CO_2 and C_2H_2 are almost identical, the efficient separation of the CO_2/C_2H_2 mixture cannot be realized simply by tuning the pore size, unlike other gaseous mixtures, such as CO_2/N_2 and alkyne/alkene.[33,34] It is worth noting that there is a key difference in electrostatic potentials (ESPs) and quadrupole moments of CO_2 and C_2H_2. Therefore, it is significant to construct specific functional binding sites within the MOFs that could achieve inverse CO_2-selective behavior for the effective purification of C_2H_2. It is generally believed that ultramicroporous adsorbents featuring a compact pore space and positively charged distribution could maximize the inverse selectivity and decrease the C_2H_2 sorption.[35] Additionally, to enhance the stability of MOFs and solve the issue of the trade-off between CO_2 uptake and CO_2/C_2H_2 separation selectivity, inspired by pore functionality within MOFs, we propose the immobilization of the polar group strategy to target the one-step purification of C_2H_2 without an extra desorption process. Based on the difference of electric quadrupole between CO_2 and C_2H_2 molecules, we speculate that the methyl group (−CH_3)-functionalized pore channel could tune the pore environment to strengthen the recognition capability of guests and further enhance the CO_2−framework interaction and decrease the C_2H_2−framework interaction, i.e., the methyl-functionalized MOF could tailor the pore size to the optimal range and have moderate noncovalent van der Waals interactions with CO_2 molecules for sufficient CO_2 affinity. Moreover, the optimal pore size with functional sites could effectively address the trade-off of uptake and selectivity. At the same time, introduction of hydrophobic −CH_3 functional groups could enhance the chemical stability, especially water stability, of the framework, which may be a one-stone-two-bird strategy. In this regard, we successfully achieved the target of inverse CO_2 selection for the CO_2/C_2H_2 mixture via the construction of a methyl group-functionalized pore environment, based on pore chemistry and crystal engineering, to directly obtain high-purity C_2H_2. We chose Zn-ox-trz (ox, oxalate; trz, 1,2,4-triazole) as a prototype MOF, and the immobilization of the methyl group into the organic ligand not only changes the pore environment but also provides the binding affinity sites to enhance CO_2−MOF interactions. As expected, the methyl-functionalized **Zn-ox-mtz** (mtz, 3-methyl-1,2,4-triazole) exhibits the preferential adsorption of CO_2 over C_2H_2. Gas sorption measurements reveal that **Zn-ox-mtz** is an excellent CO_2-selective MOF material with a high CO_2/C_2H_2 uptake ratio of 12.6 and a selectivity of 1064.9 at ambient conditions, establishing a new benchmark material for reverse-selective CO_2/C_2H_2 separation, which is much higher than the prototype MOF with a larger pore. **Zn-ox-mtz** provides the optimal pore environment to accommodate CO_2, and CO_2 was captured into the pores through the robust host−guest interactions by the methyl groups from organic ligands, which is evidenced by molecular simulations. In addition, the column breakthrough experiments and simulations confirm the state-of-the-art CO_2/C_2H_2 separation performance with a benchmark C_2H_2 productivity of 2091 mmol kg^{-1}, and the cycling breakthrough experiments and sorption measurements

https://doi.org/10.1021/jacs.3c03265
J. Am. Chem. Soc. 2023, 145, 13901−13911

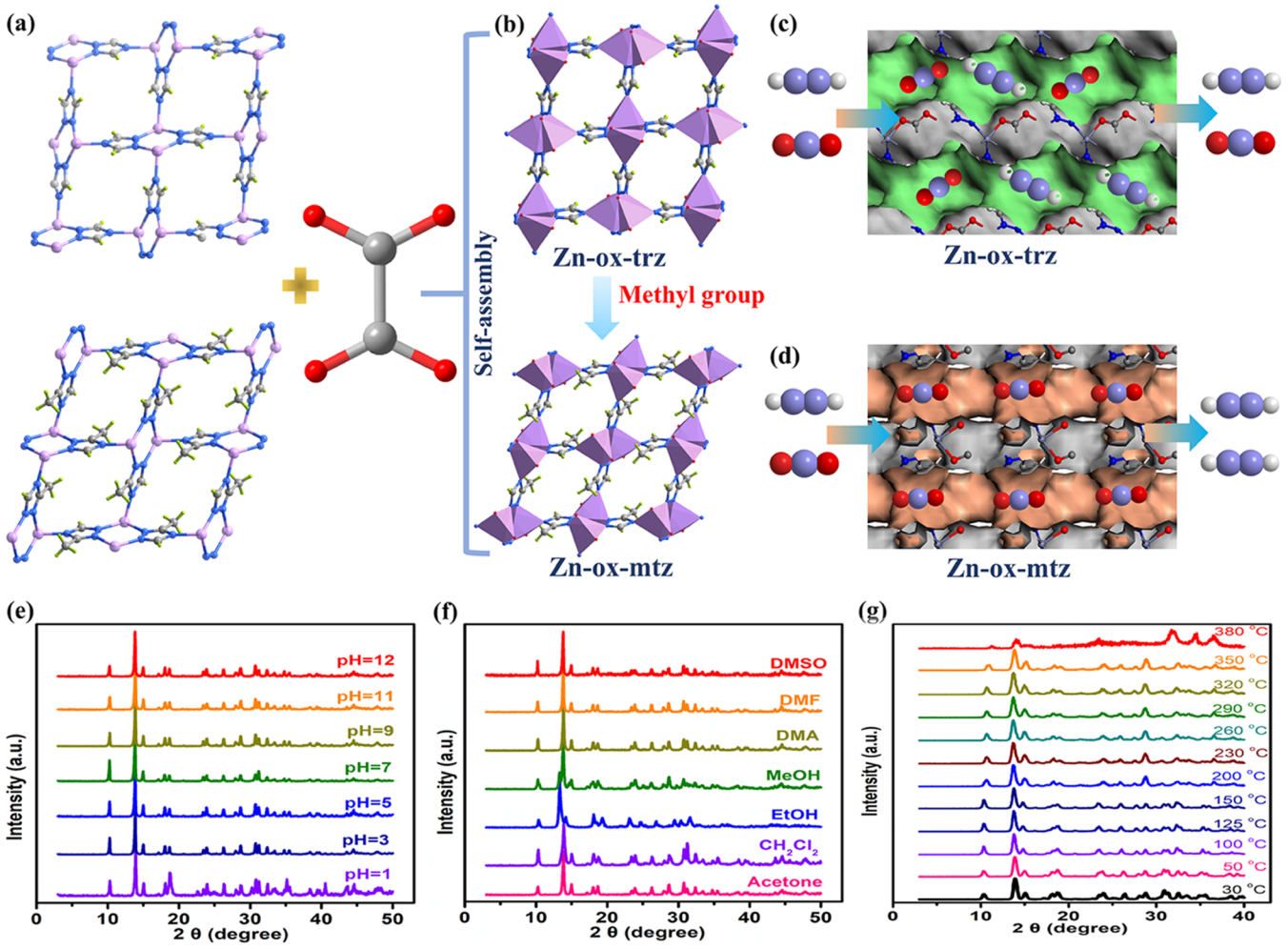

Figure 1. (a) View of the two-dimensional (2D) zinc triazolate layer and oxalate unit. (b) Three-dimensional pillared-layer frameworks along the *a* axis. (c) One-dimensional channel structure of Zn-ox-trz (the channels are expressed in green; Zn-ox-trz exhibits a low recognition for guest molecules: both CO_2 and C_2H_2 could pass through). (d) One-dimensional channel structure of **Zn-ox-mtz** (the channels are expressed in orange; the methyl-functionalized MOF could effectively improve the recognition of guest molecules: CO_2 molecules are trapped and the high-purity C_2H_2 stream could be straight obtained; Zn, lavender; C, light gray; N, blue; H, light green; O, red). PXRD patterns of **Zn-ox-mtz** samples: (e) soaking in different pH aqueous solvents for 14 days; (f) soaking in different organic solvents for 14 days. (g) In situ VT-PXRD from room temperature to 380 °C under an Ar atmosphere.

further prove the good recyclability and stability. These results make **Zn-ox-mtz** a benchmark adsorbent for high-efficiency CO_2/C_2H_2 separation, which is extremely sought-after in the industrial process yet has been scarcely reported. Moreover, the greatly stable framework of **Zn-ox-mtz** further showcases its promising practical application as a C_2H_2 splitter for industrial manufacture.

RESULTS AND DISCUSSION

Given the impact of pore sizes, environments, and physiochemical properties of the pore surface on the sorption behavior as well as the importance of MOFs with high stability, the tunable and stable Zn-ox-trz was selected as a prototype MOF material. To introduce bulky organic moieties for further adjusting the pore chemistry, the ligand with the methyl group was used to build an isoreticular framework affording **Zn-ox-mtz**. The Zn-ox-trz sample was easily synthesized by a solvothermal method in light of the previously reported method with some modifications.[33] High-quality single crystals of **Zn-ox-mtz** could be obtained through the reaction of 3-methyl-1*H*-1,2,4-triazole, oxalate, and $ZnCO_3$ in a butanol solution at 453 K for 3 days. Single-crystal X-ray diffraction (SCXRD) revealed that **Zn-ox-mtz** crystallized in the *P*21/*c* space group, which is isostructural to Zn-ox-trz. As shown in Figure 1, in both MOFs, each Zn ion adopts a five-coordinated configuration with a distorted trigonal bipyramidal geometry, which is coordinated with three nitrogen atoms from tridentately bridging triazole units and two oxygen atoms from bidentately chelating oxalate units. **Zn-ox-mtz** is formed by the layers of CH_3-decorated 1,2,4-triazole-bridged Zn ions pillared in an out-of-plane form by the oxalate units to obtain a three-dimensional (3D) framework and a one-dimensional (1D) pore structure; the same is true of Zn-ox-trz, except for 1,2,4-triazole replacing the CH_3-decorated 1,2,4-triazole (Figure 1a,b). Especially, compared to Zn-ox-trz, **Zn-ox-mtz** possesses free methyl groups lining the pore channels, which decreases the pore apertures to 5.30 × 3.50 $Å^2$ from 5.20 × 5.70 $Å^2$. The insertion of the methyl group tailors the pore diameter to the optimal range for the adsorption of CO_2 molecules and provides potential binding sites. Thus, the methyl-functionalized MOF not only decreases the pore apertures but also facilitates the host−guest interactions in

https://doi.org/10.1021/jacs.3c03265
J. Am. Chem. Soc. 2023, 145, 13901−13911

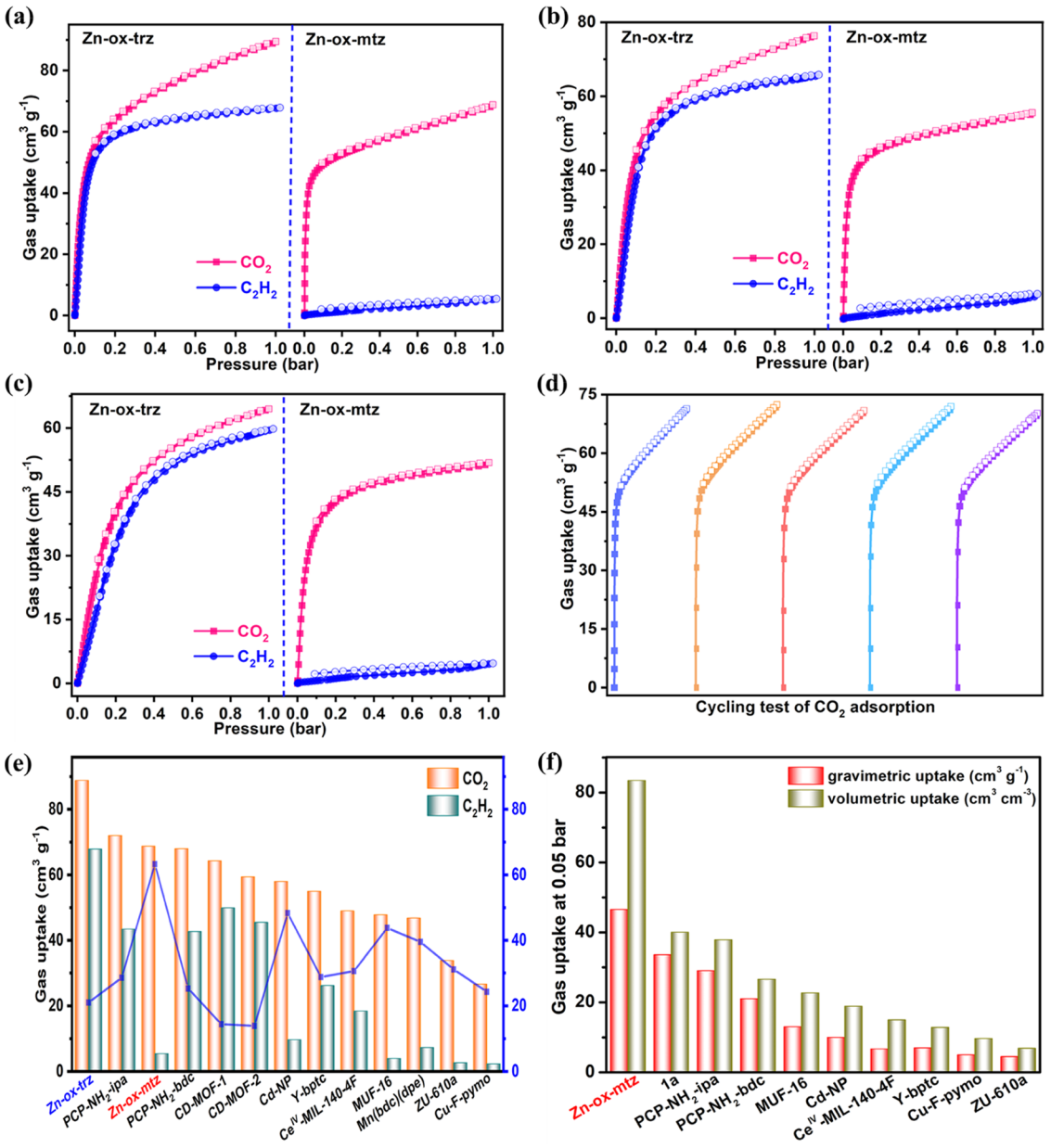

Figure 2. Gas sorption isotherms of Zn-ox-trz (left) and **Zn-ox-mtz** (right) (a) at 298 K, (b) at 313 K, and (c) at 333 K. (d) Cycling test of CO_2 sorption measurements on **Zn-ox-mtz** at 298 K from 0 to 1.0 bar. (e) Adsorption capacity of CO_2 and C_2H_2 for representative CO_2-selective adsorbents at 298 K and 1.0 bar (the blue line indicates the adsorption capacity difference between CO_2 and C_2H_2, i.e., blue line value = CO_2 uptake − C_2H_2 uptake). (f) Comparison of CO_2 uptake at 298 K and 0.05 bar among different CO_2-selective materials.

the compact space, which transfers the low recognition ability for guest gases to high recognition ability for adsorbed gases (Figure 1c,d). The bulk phase purity and crystallinity of Zn-ox-trz and **Zn-ox-mtz** were verified by powder X-ray diffraction (PXRD) (Figures S1 and S2). The surface morphologies of Zn-ox-trz and **Zn-ox-mtz** were analyzed by scanning electron microscopy (SEM), which indicated that these MOFs are sheet-like (Figures S13 and S14).

From the perspective of practical application, considering the industrial implementation is usually under humid or acidic conditions, the adsorbent materials should possess high water and chemical stabilities. Thus, the chemical stability of **Zn-ox-mtz** toward acid, water, base solutions, and organic solvents was examined. As shown in Figure 1e,f, **Zn-ox-mtz** exhibits structural stability of aqueous solutions with different pH values (pH = 1−12) and different organic solvents for 14 days, which confirmed its highly robust nature for practical implementation under harsh conditions. In addition, the thermal stability of **Zn-ox-mtz** was also investigated by thermogravimetric analysis (TGA) and in situ variable-temperature powder X-ray diffraction (VT-PXRD); the results of TGA and VT-PXRD indicated that **Zn-ox-mtz** was thermally stable until 600 K (Figures 1g and S15). Obviously, **Zn-ox-mtz** exhibits excellent thermal and chemical stability. The ultramicroporous framework and high stability make the methyl-functionalized **Zn-ox-mtz** an ideal platform for gas separation implementations.

Before evaluating the permanent porosity, the activated samples for two Zn-MOFs could be directly obtained at 373 K for 12 h under a high vacuum. The pore features of the

https://doi.org/10.1021/jacs.3c03265
J. Am. Chem. Soc. 2023, 145, 13901−13911

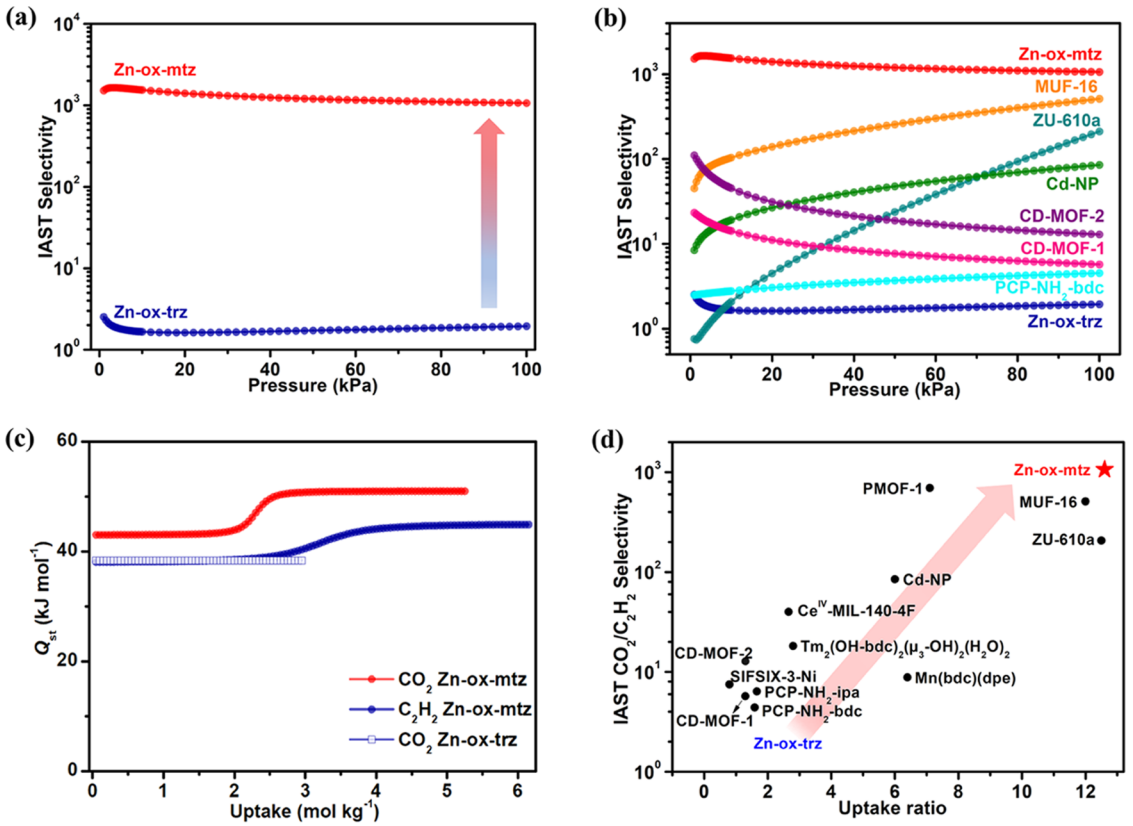

Figure 3. (a) Predicted IAST selectivity curves for an equimolar CO_2/C_2H_2 mixture at 298 K. (b) Comparison of equimolar CO_2/C_2H_2 mixture separation selectivity at 298 K. (c) Isosteric heat of adsorption for Zn-ox-trz and **Zn-ox-mtz**. (d) Comparison of the CO_2/C_2H_2 uptake ratio and equimolar CO_2/C_2H_2 selectivity with popular CO_2-selective adsorbents at 298 K and 1.0 bar.

activated Zn-MOFs were obtained through CO_2 sorption experiments at 195 K. It could be seen from Figures S3 and S4 that these MOF materials exhibit a completely reversible type I sorption behavior. The saturated CO_2 adsorption capacity of **Zn-ox-mtz** is 100.16 $cm^3\ g^{-1}$, which is lower than that of Zn-ox-trz (132.65 $cm^3\ g^{-1}$) owing to the introduction of the $-CH_3$ group. The Brunauer–Emmett–Teller surface area of **Zn-ox-mtz** is decreased from 466 $m^2\ g^{-1}$ in Zn-ox-trz to 344 $m^2\ g^{-1}$ according to the CO_2 adsorption isotherm (Figures S5 and S6). Additionally, the pore volume calculated on the basis of the saturated CO_2 uptake also decreased from 0.28 $cm^3\ g^{-1}$ in Zn-ox-trz to 0.21 $cm^3\ g^{-1}$.

Considering the interesting pore chemistry as well as the suitable pore size, the single-component gas sorption isotherms of CO_2 and C_2H_2 for Zn-ox-trz and **Zn-ox-mtz** were measured at 298, 313, and 333 K in the pressure range of 0.0–1.0 bar, respectively. As shown in Figure 2a–c, although both Zn-ox-trz and **Zn-ox-mtz** show an inverse CO_2-selective adsorption behavior, they exhibited an apparent difference in the sorption performance for C_2H_2 and CO_2. The CO_2 adsorption capacity of **Zn-ox-mtz** is 68.78 $cm^3\ g^{-1}$ (3.07 mmol g^{-1}) at 298 K and 1.0 bar, which is slightly lower than that of Zn-ox-trz (89.49 $cm^3\ g^{-1}$ or ~4.0 mmol g^{-1}). More significantly, **Zn-ox-mtz** exhibits a negligible C_2H_2 uptake with 5.46 $cm^3\ g^{-1}$ (0.24 mmol g^{-1}), which is much lower than that of Zn-ox-trz with 67.85 $cm^3\ g^{-1}$ (3.03 mmol g^{-1}). Such an obvious adsorption difference on **Zn-ox-mtz** gives rise to a high CO_2/C_2H_2 uptake ratio with the value of 12.6, which is 9.5 times higher than that of Zn-ox-trz, establishing a new benchmark for CO_2-selective MOFs for CO_2/C_2H_2 separation under ambient conditions (Figure 2e). We further notice that the gravimetric CO_2 uptake of **Zn-ox-mtz** at ambient conditions is higher than or comparable to those of most benchmark CO_2-selective MOFs such as Cd–NP (58.0 $cm^3\ g^{-1}$),[35] Ce^{IV}-MIL-140-4F (48.9 $cm^3\ g^{-1}$),[36] Cu–F-pymo (26.6 $cm^3\ g^{-1}$),[31] MUF-16 (47.8 $cm^3\ g^{-1}$),[37] ZU-610a (33.8 $cm^3\ g^{-1}$),[38] and PCP–NH_2-bdc (68 $cm^3\ g^{-1}$).[39] Specially, the volumetric storage capacity is also a key parameter to evaluate the actual separation process, which could take full advantage of the packed-bed space and decrease the energy consumption of the regeneration process. In terms of volumetric storage capacity, **Zn-ox-mtz** exhibits a remarkable volumetric adsorption capacity for CO_2 with 123.32 cm^3; such a high volumetric uptake is significantly higher than that of CO_2-selective adsorbents, including but not limited to MUF-16 (74.7 $cm^3\ cm^{-3}$),[37] Ce^{IV}-MIL-140-4F (110.3 $cm^3\ cm^{-3}$),[36] SIFSIX-3-Ni (98.4 $cm^3\ cm^{-3}$),[7] CD-MOFs (60.4 $cm^3\ cm^{-3}$),[32] and PCP–NH_2-ipa (93.6 $cm^3\ cm^{-3}$).[39] Obviously, **Zn-ox-mtz** displays an excellent trade-off between the gravimetric and volumetric adsorption capacities, which is a key scientific problem and of industrial relevance. In addition, to the best of our knowledge, the excellent uptake ratio is superior to all of those reported benchmark CO_2-selective porous adsorbents such as Cd–NP (6.0),[35] Ce(IV)-MIL-140-4F (2.65),[36] PCP–NH_2-bdc (1.59) and PCP–NH_2-ipa (1.6),[39] PMOF-1 (7.1),[40] and een-MOF (2.64)[41] (Table S4, Supporting Information). Significantly, unlike most CO_2-selective adsorbent materials that present limited CO_2 uptake in the low-pressure region, the CO_2 uptake on **Zn-ox-mtz** increases sharply. At 298 K and 0.05 bar, the CO_2 uptake reaches 46.54 $cm^3\ g^{-1}$ (2.08 mmol g^{-1}), which is

https://doi.org/10.1021/jacs.3c03265
J. Am. Chem. Soc. 2023, 145, 13901–13911

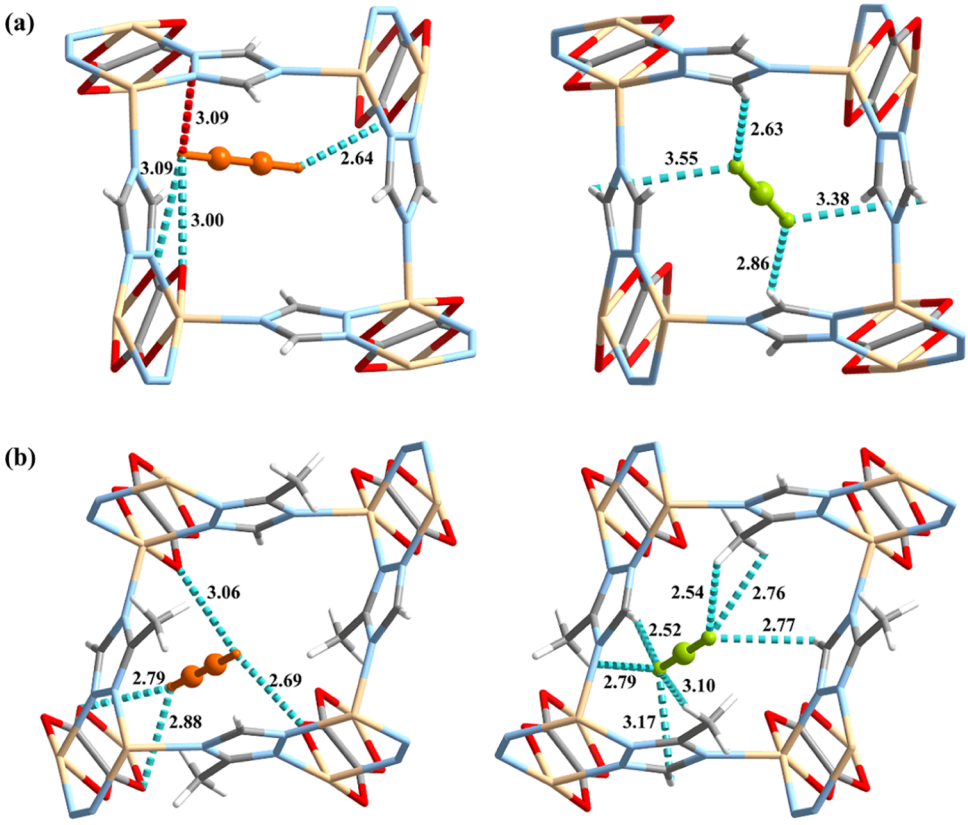

Figure 4. Adsorption binding sites in (a) Zn-ox-trz for C_2H_2 (left) and CO_2 (right), (b) C_2H_2 (left) and CO_2 (right) molecule binding sites in **Zn-ox-mtz** by theoretical calculations. Distances are given in Å.

apparently higher than those of PCP−NH_2-bdc (21 $cm^3\ g^{-1}$)[39] and MUF-16 (13 $cm^3\ g^{-1}$).[37] To the best of our knowledge, this uptake level is the highest among all reported CO_2-selective MOF materials (Figure 2f). Such an excellent gas adsorption capacity could endow **Zn-ox-mtz** with a prominent capacity to capture trace amounts of CO_2 contaminants, which is vital in industrial implementation. Continuous CO_2 sorption experiments on **Zn-ox-mtz** were performed to assess its cycling stability. After five cycles, **Zn-ox-mtz** showed no obvious reduction in its CO_2 uptake (Figure 2d).

To evaluate the separation potential of Zn-ox-trz and **Zn-ox-mtz** for the CO_2/C_2H_2 mixture, the ideal adsorbed solution theory (IAST) was used to assess the adsorptive selectivity toward the equimolar CO_2/C_2H_2 mixture. As shown in Figure 3a, Zn-ox-trz exhibits a low CO_2/C_2H_2 selectivity of 1.9 at 298 K and 1.0 bar owing to the very similar adsorption isotherms of CO_2 and C_2H_2. After the insertion of the $-CH_3$ group into the structure, **Zn-ox-mtz** exhibits a dramatically enhanced CO_2/C_2H_2 selectivity of 1064.9, which is 560 times higher than that of Zn-ox-trz. This selectivity value under the same conditions is greatly higher than that of the most reported CO_2-selective materials such as MUF-16 (510),[37] SIFSIX-3-Ni (7.5),[7] $[Tm_2(OH\text{-}bdc)_2(\mu_3\text{-}OH)_2(H_2O)_2](18.2)$,[42] Cd−NP (85),[35] and PCP−NH_2-ipa (6.4)[39] (Figure 3b). It is worth noting that the calculated CO_2/C_2H_2 separation selectivity serves as a qualitative description of the mixture separation capacity, but it is only for qualitative comparison. In addition, the coverage-dependent isosteric heats of adsorption (Q_{st}), which quantitatively evaluates the interactions between adsorbed gas and the framework, for CO_2 on **Zn-ox-mtz** was calculated to be 43.02 kJ mol^{-1} at near-zero coverage (Figure 3c). The Q_{st} values of Zn-ox-trz for CO_2 and C_2H_2 are 38.09 and 38.39 kJ mol^{-1}, respectively, which is in good agreement with the sorption isotherms. In addition, compared to Zn-ox-trz, the higher heat of adsorption of CO_2 for **Zn-ox-mtz** indicates a higher binding affinity, which can be seen in the adsorption isotherm in the low-pressure region (Figure S17). The adsorption and separation properties are further evaluated in multiple dimensions including CO_2/C_2H_2 selectivity, CO_2/C_2H_2 uptake ratio, and CO_2 uptake; **Zn-ox-mtz** exhibits excellent performance among these evaluation criteria (Figures S18 and S19). We realize that the combination of high adsorption capacity and good selectivity is still rare in MOF adsorbents, and previously reported CO_2-selective MOFs generally display either low capacity or poor selectivity.[7,31,32,38,39,43,44] With adsorption capacity and selectivity as parallel goals, **Zn-ox-mtz** shows the best trade-off between them, establishing a new benchmark for reverse CO_2/C_2H_2 adsorption (Figure 3d). By virtue of the outstanding CO_2 adsorption capacity, moderate isosteric heats of adsorption, benchmark uptake ratio, and high inverse selectivity, **Zn-ox-mtz** could be the most promising porous adsorbent for the direct one-step purification of C_2H_2 from the CO_2/C_2H_2 mixture.

To gain a profound understanding on the effect of the incorporation of the methyl group on the pore chemistry and the origin of markedly enhanced gas selectivity, grand canonical Monte Carlo (GCMC) simulations on Zn-ox-trz and **Zn-ox-mtz** were carried out to investigate the host−guest interactions between the framework and the adsorbed gas molecules. As outlined in Figure 4a, in Zn-ox-trz, each C_2H_2 molecule interacts with three oxygen atoms from two oxalate

https://doi.org/10.1021/jacs.3c03265
J. Am. Chem. Soc. 2023, 145, 13901−13911

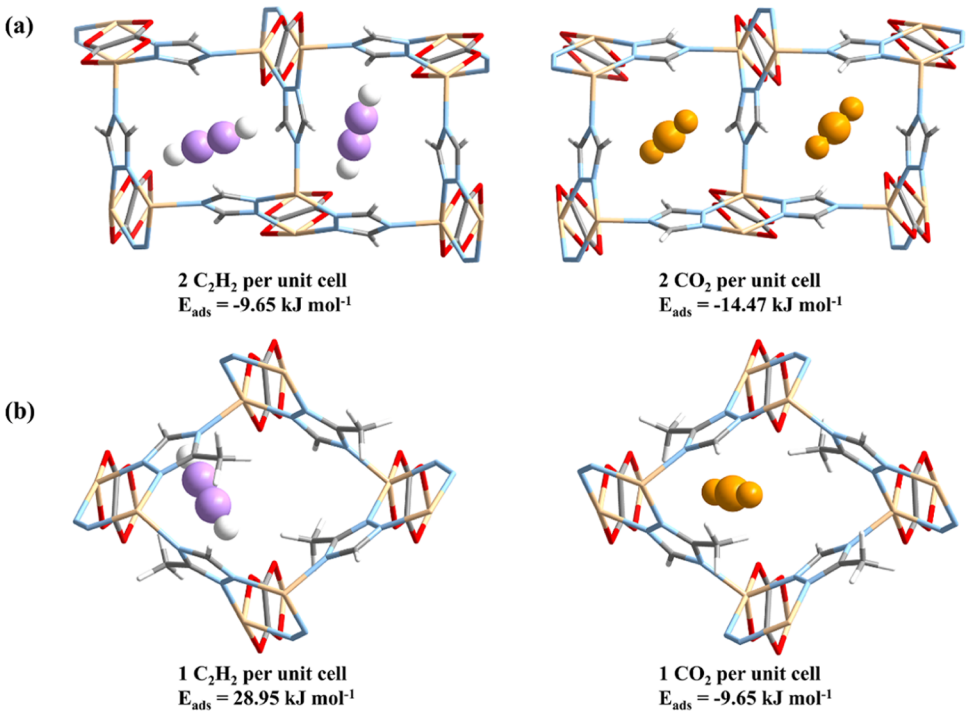

Figure 5. Adsorption energies of (a) C_2H_2 (left) and CO_2 (right) in Zn-ox-trz and (b) C_2H_2 (left) and CO_2 (right) in **Zn-ox-mtz** by density functional theory calculations.

ligands to form three C−H···O interactions (H−O, 2.64−3.09 Å) and one nitrogen atom from the triazole ligand to form one C−H···N interaction (H−N, 3.09 Å), and each CO_2 molecule interacts with four triazole ligands to form four C−H···O interactions (H−O, 2.63−3.55 Å). Thus, the similar host−guest interactions result in a close adsorption behavior and low separation potential. After methyl group functionalization, the pore environment becomes compact; in addition, the free methyl groups lining the pore channels provide binding bites for CO_2 molecules. As shown in Figure 4b, the C_2H_2 molecule adsorbed in **Zn-ox-mtz** interacts only with three oxalates and four oxygen atoms to form four C−H···O interactions (H−O, 2.69−3.06 Å), while the CO_2 molecule interacts not only with three hydrogens of the triazole to form three C−H···O interactions (H−O, 2.52, 2.77, and 3.17 Å) but also with three $-CH_3$ groups to form four C−H···O interactions (H−O, 2.54, 2.76, 2.79, and 3.10 Å). From another point of view, to clearly explain the reason for the decrease in C_2H_2 uptake in **Zn-ox-mtz**, we further mapped the ESP of gas molecules and pore surfaces of MOFs using density functional theory (DFT) calculations (Figure S7). As shown in Figure S7a,b, it is obvious that CO_2 and C_2H_2 possess opposite electrostatic potentials. In the prototype and methyl-functionalized MOFs, the positive potential is found on the hydrogen atom in the ligands and near the Zn center, respectively, as well as a negative potential is found near the oxygen and nitrogen atoms of the ligands (Figure S7c,d). Compared to prototype MOF, methyl-functionalized MOF exhibits a much positively charged pore surface owing to more hydrogen atoms of methyl groups lining the pore channel. In the prototype MOF, Zn-ox-trz has a wide open pore space, where both C_2H_2 and CO_2 could achieve their own optimal adsorption configurations in different orientations. After methyl insertion, the pore space becomes more compact and more hydrogen lines the channel, forming the positively charged pore environment. The dimensions of the **Zn-ox-mtz** pores are well matched to CO_2 molecule sizes, which allows the CO_2 molecules to be encompassed by multiple noncovalent contacts, and these contacts support the CO_2-selective adsorption behavior since the electrostatic potential of CO_2 is complementary to the methyl-functionalized pore surface potential (Figure S7a,d). However, C_2H_2 is polarized oppositely to CO_2 and it is electrostatically repelled by the methyl groups in **Zn-ox-mtz** (Figure S7b,d). In short, compared to the prototype MOF, ultramicroporous characteristics featuring a compact pore space and positive charge distribution at the pore wall of **Zn-ox-mtz** could significantly decrease the C_2H_2 adsorption capacity and maximize the inverse CO_2/C_2H_2 selectivity. Evidently, the immobilization of $-CH_3$ groups allows the framework to bind more strongly with CO_2 compared with C_2H_2 within the pore channel, thus leading to the significant adsorption performance difference between CO_2 and C_2H_2.

Density functional theory calculations were performed to further access the adsorption energy of guest molecules (C_2H_2 and CO_2) in prototype Zn-ox-trz and methyl-functionalized **Zn-ox-mtz** (the detailed calculations are demonstrated in the Supporting Information). According to the defined formula, the more negative the adsorption energy value, the stronger the binding affinity is on the same adsorbent. Considering the adsorbed molecule quantity in one unit cell from an experimental perspective, the calculated averages of the adsorption energy of C_2H_2 and CO_2 on Zn-ox-trz are −9.65 and −14.47 kJ mol^{-1} (Figure 5a), respectively, indicating a stronger binding affinity to CO_2 over C_2H_2, which is in good agreement with the adsorption behaviors. In the $-CH_3$-functionalized **Zn-ox-mtz**, the calculated adsorption energies of C_2H_2 and CO_2 are 28.95 and −9.65 kJ mol^{-1} (Figure 5b), respectively, and this result suggests that the binding affinity between the framework and C_2H_2 is very weak and there is a stronger host−guest interaction between CO_2 and the

https://doi.org/10.1021/jacs.3c03265
J. Am. Chem. Soc. 2023, 145, 13901−13911

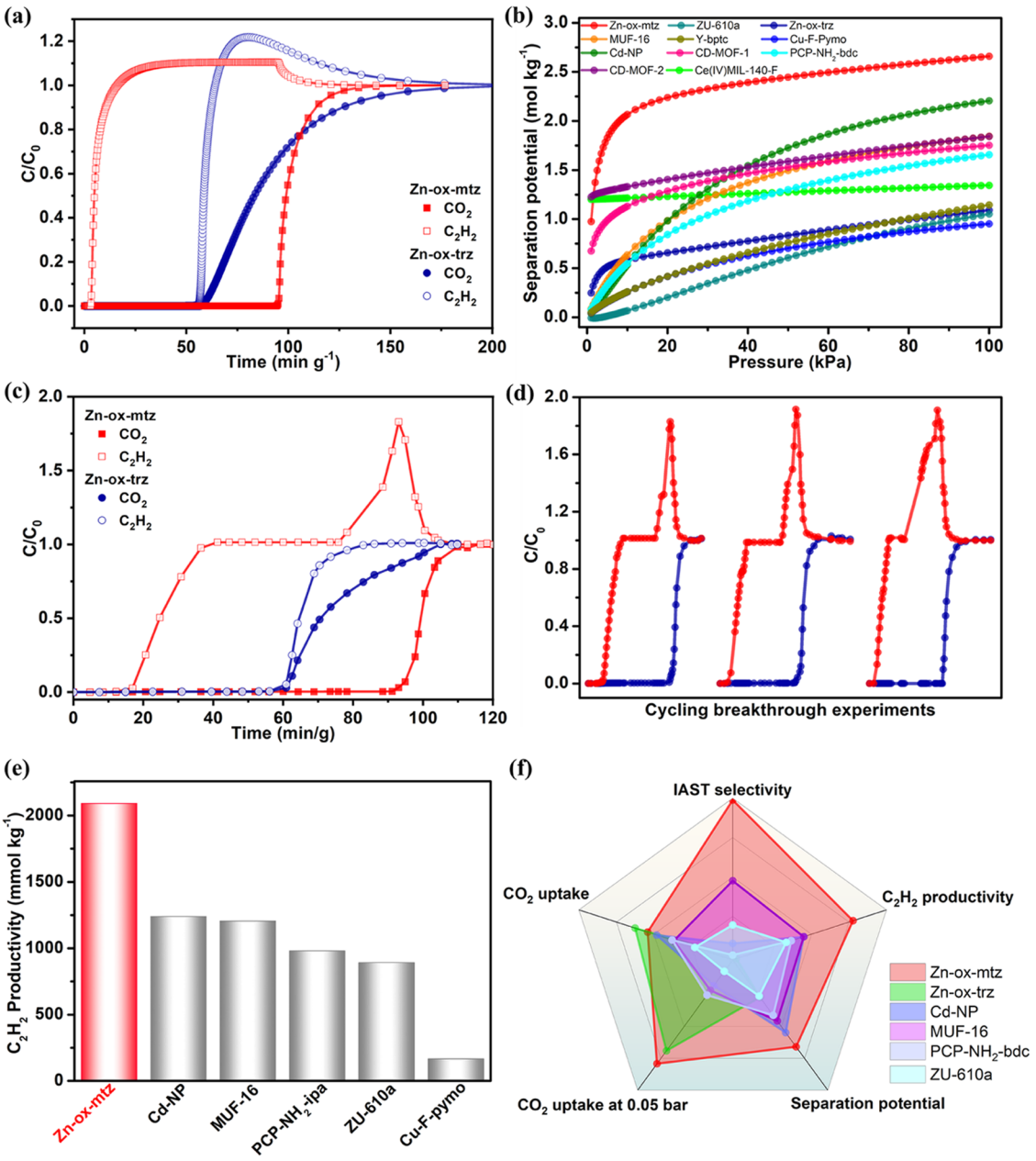

Figure 6. (a) Simulated breakthrough curves for an equimolar CO_2/C_2H_2 mixture in the fixed bed packed with Zn-ox-trz and **Zn-ox-mtz** at 298 K and 1.0 bar. (b) Separation potential of the selected MOF materials for the equimolar CO_2/C_2H_2 mixture. (c) Experimental column breakthrough curves for the equimolar CO_2/C_2H_2 mixture on Zn-ox-trz and **Zn-ox-mtz** at 298 K and 1.0 bar. (d) Cycling tests of the equimolar CO_2/C_2H_2 mixture on **Zn-ox-mtz** at 298 K and 1.0 bar. (e) Comparison of C_2H_2 productivity with the reported benchmark porous materials at ambient conditions. (f) Comparison of the comprehensive separation performance with reported excellent reverse CO_2-selective MOFs.

skeleton. This could be attributed to the suitable binding sites for CO_2 and the strong recognition capacity for the CO_2/C_2H_2 mixture, provided by the $-CH_3$-functionalized framework. The different adsorption energy behaviors on Zn-ox-trz and **Zn-ox-mtz** indicate the profound effect of immobilization of the $-CH_3$ group on CO_2 and C_2H_2 adsorption performance.

To effectively validate the positive impact of methyl groups on CO_2/C_2H_2 separation, transient breakthrough simulations for an equimolar CO_2/C_2H_2 mixture on Zn-ox-trz and **Zn-ox-mtz** in a fixed bed were carried out at 298 K and 1.0 bar (Figure 6a). The methodology used in the transient breakthrough simulations is the same as described by Krishna.[45,46] A summary of the methodology is also included in the Supporting Information. The results displayed that Zn-ox-trz presented weak CO_2/C_2H_2 separation capacity and **Zn-ox-mtz** accomplished highly efficient separation. The separation potential, as a combined metric for adsorption capacity and selectivity,[47,48] was performed to qualitatively prove their separation performances. As shown in Figure 6b, the amounts of pure C_2H_2 that could be recovered by **Zn-ox-mtz** reached up to 2.66 mol kg^{-1} for the equimolar CO_2/C_2H_2 mixture, greatly surpassing the performance of other selected reverse adsorbents. Next, to further access the practical CO_2/C_2H_2 separation capacity of **Zn-ox-mtz**, dynamic column breakthrough experiments were performed, where the equimolar CO_2/C_2H_2 gas mixture flowed over the Zn-ox-trz and **Zn-ox-mtz** packed column at the mass flow rate of 2 mL min^{-1} under ambient conditions. Because of the low CO_2/C_2H_2 separation

https://doi.org/10.1021/jacs.3c03265
J. Am. Chem. Soc. 2023, 145, 13901−13911

performance, Zn-ox-trz could not remove CO_2 from the equimolar CO_2/C_2H_2 binary mixture to produce polymer-grade C_2H_2 in the effluent stream (Figure 6c). In contrast, a clean separation of the CO_2/C_2H_2 mixture was presented with a great separation window, and an outstanding direct one-step purification of C_2H_2 could be achieved with the **Zn-ox-mtz**. The breakthrough interval time between CO_2 and C_2H_2 is approx. 78 min g^{-1}, which exceeds that of top-performing adsorbents such as Cd−NP (15 min g^{-1})[35] and ZU-610a (28 min g^{-1}) under the same conditions.[38] The C_2H_2 gas was first eluted with high purity (>99.6%) from the packed column on **Zn-ox-mtz**, giving a highly excellent C_2H_2 productivity of 2091 mmol kg^{-1} of the adsorbent material. The C_2H_2 productivity of **Zn-ox-mtz** is state-of-the-art in the CO_2-selective materials, much higher than that on benchmark MOFs Cu−F-pymo (166 mmol kg^{-1}),[31] PCP−NH_2-ipa (980 mmol kg^{-1}),[39] and Cd−NP (1240 mmol kg^{-1})[35] (Figure 6e). CO_2 gas was trapped as an impurity in the packed column for a long time with dynamic adsorption amounts of 119 cm^3 cm^{-3}, which was in accordance with the CO_2 sorption isotherms; in addition, this dynamic capacity of CO_2 is higher than the previously reported excellent inverse selective materials such as Cd−NP (38 cm^3 cm^{-3})[35] and ZJU-610a (43 cm^3 cm^{-3}).[38] As a result, **Zn-ox-mtz** exhibits a high separation factor for an equimolar CO_2/C_2H_2 mixture with the value of 6.28 at ambient conditions, which was calculated from breakthrough experiments and reflects the actual separation performance. This separation factor value is higher than or comparable to those of Ce(IV)-MIL-140-4F (4.9),[36] NH_4-IM (4.6), and NH_4-MM (6.5).[49] Furthermore, multiple equimolar CO_2/C_2H_2 gas mixture breakthrough experiments were carried out, which indicates that **Zn-ox-mtz** could maintain a good CO_2 retention time and C_2H_2 productivity (Figure 6d), suggesting its good recyclability for this challenging CO_2/C_2H_2 separation.

For industrial implementations of CO_2/C_2H_2 separation, the ideal CO_2-selective adsorbent material should display several properties, including (i) high CO_2 uptake capacity, (ii) good CO_2/C_2H_2 selectivity, (iii) excellent thermal and chemical stability, (iv) high C_2H_2 productivity, (v) high uptake in a low-pressure region, and (vi) moderate isosteric heats of adsorption. We have shown that **Zn-ox-mtz** could meet all of these criteria, while other CO_2-selective MOFs have better presented one or more of the properties mentioned above. In point-of-separation performance, **Zn-ox-mtz** exhibits the record C_2H_2 productivity with 2091 mmol kg^{-1} among other state-of-the-art MOFs, establishing a new benchmark for inverse CO_2-selective MOFs. In addition, **Zn-ox-mtz** displays excellent CO_2 uptake and CO_2/C_2H_2 selectivity, especially its CO_2 uptake in the low-pressure area is superior to current excellent inverse CO_2-selective materials (Table S4). Poor chemical stability, especially water stability, of MOFs is still a drawback for their practical application. In this regard, the immobilization of the methyl group could dramatically improve the hydrophobicity, and **Zn-ox-mtz** shows good chemical stability toward water, acid, and base. In comprehensive consideration of the CO_2 adsorption capacity, CO_2 uptake in a low-pressure area, CO_2/C_2H_2 selectivity, C_2H_2 productivity, separation potential, and framework stability, **Zn-ox-mtz** displays the best one-step separation performance for the CO_2/C_2H_2 mixture compared to that of the reported inverse CO_2-selective adsorbents in references (Figure 6f). These advances enable **Zn-ox-mtz** to become one ideal adsorbent for challenging CO_2/C_2H_2 separation.

CONCLUSIONS

In summary, we propose a feasible approach to explore CO_2-selective MOF materials for a superior separation strategy to advance C_2H_2 production. By virtue of pore chemistry and crystal engineering, we dexterously achieved efficient inverse CO_2/C_2H_2 adsorption and separation via the immobilization of a methyl group into the prototype MOF. This specific capture of CO_2 over C_2H_2 is mainly attributed to methyl-functionalized **Zn-ox-mtz**, which provides high recognition of CO_2 molecules through multiple van der Waals interactions, thus establishing the benchmark inverse CO_2/C_2H_2 separation and record C_2H_2 production. As evidenced by sorption measurements, theoretical calculations, and breakthrough experiments, high-purity C_2H_2 could be directly harvested from the CO_2/C_2H_2 mixture via a single adsorption process with a high production of 2091 mmol kg^{-1}. Together with cheap precursors, high framework stability, and excellent separation capacity, **Zn-ox-mtz** would be a promising candidate adsorbent for the CO_2/C_2H_2 separation process. This study elaborates on the effectiveness of optimized pore environments through introduction of polar groups within MOFs, which will open more opportunities to develop advanced porous solid materials with dramatic separation performance and inspire the construction of MOFs aimed at the separation process with similar physical properties in an adsorptive separation field.

ASSOCIATED CONTENT

Supporting Information

The Supporting Information is available free of charge at https://pubs.acs.org/doi/10.1021/jacs.3c03265.

Full experimental details, including material synthesis, crystal data, PXRD patterns, TGA curves, SEM images, CO_2 sorption data, grand canonical Monte Carlo simulations, density functional theory calculations, breakthrough experiments, transient breakthrough simulations, and comparison of CO_2-selective adsorbents (PDF)

Accession Codes

CCDC 2248518 contains the supplementary crystallographic data for this paper. These data can be obtained free of charge via www.ccdc.cam.ac.uk/data_request/cif, or by emailing data_request@ccdc.cam.ac.uk, or by contacting The Cambridge Crystallographic Data Centre, 12 Union Road, Cambridge CB2 1EZ, UK; fax: +44 1223 336033.

AUTHOR INFORMATION

Corresponding Author

Tong-Liang Hu − *School of Materials Science and Engineering, National Institute for Advanced Materials, Nankai University, Tianjin 300350, China*; orcid.org/0000-0001-9619-9867; Email: tlhu@nankai.edu.cn

Authors

Shan-Qing Yang − *School of Materials Science and Engineering, National Institute for Advanced Materials, Nankai University, Tianjin 300350, China*

Rajamani Krishna − *Van 't Hoff Institute for Molecular Sciences, University of Amsterdam, 1098 XH Amsterdam, The Netherlands*; orcid.org/0000-0002-4784-8530

Hongwei Chen − *College of Chemistry and Chemical Engineering, Shanxi Key Laboratory of Gas Energy Efficient*

and Clean Utilization, Taiyuan University of Technology, Taiyuan 030024 Shanxi, China

Libo Li − *College of Chemistry and Chemical Engineering, Shanxi Key Laboratory of Gas Energy Efficient and Clean Utilization, Taiyuan University of Technology, Taiyuan 030024 Shanxi, China;* orcid.org/0000-0001-7147-9838

Lei Zhou − *School of Materials Science and Engineering, National Institute for Advanced Materials, Nankai University, Tianjin 300350, China*

Yi-Feng An − *School of Materials Science and Engineering, National Institute for Advanced Materials, Nankai University, Tianjin 300350, China*

Fei-Yang Zhang − *School of Materials Science and Engineering, National Institute for Advanced Materials, Nankai University, Tianjin 300350, China*

Qiang Zhang − *School of Materials Science and Engineering, National Institute for Advanced Materials, Nankai University, Tianjin 300350, China*

Ying-Hui Zhang − *School of Materials Science and Engineering, National Institute for Advanced Materials, Nankai University, Tianjin 300350, China*

Wei Li − *School of Materials Science and Engineering, National Institute for Advanced Materials, Nankai University, Tianjin 300350, China;* orcid.org/0000-0002-5277-6850

Xian-He Bu − *School of Materials Science and Engineering, National Institute for Advanced Materials, Nankai University, Tianjin 300350, China;* orcid.org/0000-0002-2646-7974

Complete contact information is available at: https://pubs.acs.org/10.1021/jacs.3c03265

Notes

The authors declare no competing financial interest.

■ ACKNOWLEDGMENTS

This work was financially supported by the National Natural Science Foundation of China (22275102) and the Natural Science Foundation of Tianjin (20JCYBJC01330).

■ REFERENCES

(1) Sholl, D. S.; Lively, R. P. Seven Chemical Separations to Change the World. *Nature* **2016**, *532*, 435−437.

(2) Wu, Y.; Weckhuysen, B. M. Separation and Purification of Hydrocarbons with Porous Materials. *Angew. Chem., Int. Ed.* **2021**, *60*, 18930−18949.

(3) Schobert, H. Production of Acetylene and Acetylene-based Chemicals from Coal. *Chem. Rev.* **2014**, *114*, 1743−1760.

(4) Fan, W.; Yuan, S.; Wang, W.; Feng, L.; Liu, X.; Zhang, X.; Wang, X.; Kang, Z.; Dai, F.; Yuan, D.; Sun, D.; Zhou, H.-C. Optimizing Multivariate Metal-Organic Frameworks for Efficient C_2H_2/CO_2 Separation. *J. Am. Chem. Soc.* **2020**, *142*, 8728−8737.

(5) Reid, C. R.; Thomas, K. M. Adsorption Kinetics and Size Exclusion Properties of Probe Molecules for the Selective Porosity in a Carbon Molecular Sieve Used for Air Separation. *J. Phys. Chem. B* **2001**, *105*, 10619−10629.

(6) Matsuda, R.; Kitaura, R.; Kitagawa, S.; Kubota, Y.; Belosludov, R. V.; Kobayashi, T. C.; Sakamoto, H.; Chiba, T.; Takata, M.; Kawazoe, Y.; Mita, Y. Highly Controlled Acetylene Accommodation in a Metal-Organic Microporous Material. *Nature* **2005**, *436*, 238−241.

(7) Chen, K.-J.; Scott, H. S.; Madden, D. G.; Pham, T.; Kumar, A.; Bajpai, A.; Lusi, M.; Forrest, K. A.; Space, B.; Perry, J. J., IV; Zaworotko, M. J. Benchmark C_2H_2/CO_2 and CO_2/C_2H_2 Separation by Two Closely Related Hybrid Ultramicroporous Materials. *Chem* **2016**, *1*, 753−765.

(8) Yang, L.; Yan, L.; Wang, Y.; Liu, Z.; He, J.; Fu, Q.; Liu, D.; Gu, X.; Dai, P.; Li, L.; Zhao, X. Adsorption Site Selective Occupation Strategy within a Metal−Organic Framework for Highly Efficient Sieving Acetylene from Carbon Dioxide. *Angew. Chem., Int. Ed.* **2021**, *60*, 4570−4574.

(9) Mukherjee, S.; Sensharma, D.; Chen, K.-J.; Zaworotko, M. J. Crystal Engineering of Porous Coordination Networks to Enable Separation of C2 Hydrocarbons. *Chem. Commun.* **2020**, *56*, 10419−10449.

(10) Rochelle, G. T. Amine Scrubbing for CO_2 Capture. *Science* **2009**, *325*, 1652−1654.

(11) Liu, S.; Han, X.; Chai, Y.; Wu, G.; Li, W.; Li, J.; da-Silva, I.; Manuel, P.; Cheng, Y.; Daemen, L. L.; Ramirez-Cuesta, A. J.; Shi, W.; Guan, N.; Yang, S.; Li, L. Efficient Separation of Acetylene and Carbon Dioxide in a Decorated Zeolite. *Angew. Chem., Int. Ed.* **2021**, *60*, 6526−6532.

(12) Furukawa, H.; Cordova, K. E.; O'Keeffe, M.; Yaghi, O. M. The Chemistry and Applications of Metal-Organic Frameworks. *Science* **2013**, *341*, No. 1230444.

(13) Hisaki, I.; Chen, X.; Takahashi, K.; Nakamura, T. Designing Hydrogen-Bonded Organic Frameworks (HOFs) with Permanent Porosity. *Angew. Chem., Int. Ed.* **2019**, *58*, 11160−11170.

(14) Nugent, P.; Belmabkhout, Y.; Burd, S. D.; Cairns, A. J.; Luebke, R.; Forrest, K.; Pham, T.; Ma, S.; Space, B.; Wojtas, L.; Eddaoudi, M.; Zaworotko, M. J. Porous Materials with Optimal Adsorption Thermodynamics and Kinetics for CO_2 Separation. *Nature* **2013**, *495*, 80−84.

(15) Waller, P. J.; Gándara, F.; Yaghi, O. M. Chemistry of Covalent Organic Frameworks. *Acc. Chem. Res.* **2015**, *48*, 3053−3063.

(16) Zhang, Z.; Ye, Y.; Xiang, S.; Chen, B. Exploring Multifunctional Hydrogen-Bonded Organic Framework Materials. *Acc. Chem. Res.* **2022**, *55*, 3752−3766.

(17) Islamoglu, T.; Chen, Z.; Wasson, M. C.; Buru, C. T.; Kirlikovali, K. O.; Afrin, U.; Mian, M. R.; Farha, O. K. Metal-Organic Frameworks against Toxic Chemicals. *Chem. Rev.* **2020**, *120*, 8130−8160.

(18) Yang, S.-Q.; Hu, T.-L. Reverse-Selective Metal-Organic Framework Materials for the Efficient Separation and Purification of Light Hydrocarbons. *Coord. Chem. Rev.* **2022**, *468*, No. 214628.

(19) Cui, W.-G.; Hu, T.-L.; Bu, X.-H. Metal-Organic Framework Materials for the Separation and Purification of Light Hydrocarbons. *Adv. Mater.* **2020**, *32*, No. 1806445.

(20) Wang, H.; Liu, Y.; Li, J. Designer Metal-Organic Frameworks for Size-Exclusion-Based Hydrocarbon Separations: Progress and Challenges. *Adv. Mater.* **2020**, *32*, No. 2002603.

(21) Zhou, D.-D.; Zhang, X.-W.; Mo, Z.-W.; Xu, Y.-Z.; Tian, X.-Y.; Li, Y.; Chen, X.-M.; Zhang, J.-P. Adsorptive Separation of Carbon Dioxide: from Conventional Porous Materials to Metal-Organic Frameworks. *EnergyChem* **2019**, *1*, No. 100016.

(22) Hong, A. N.; Yang, H.; Bu, X.; Feng, P. Pore Space Partition of Metal-Organic Frameworks for Gas Storage and Separation. *EnergyChem* **2022**, *4*, No. 100080.

(23) Han, X.; Yang, S.; Schröder, M. Porous Metal-Organic Frameworks as Emerging Sorbents for Clean Air. *Nat. Rev. Chem.* **2019**, *3*, 108−118.

(24) Peng, Y.-L.; Pham, T.; Li, P.; Wang, T.; Chen, Y.; Chen, K.-J.; Forrest, K. A.; Space, B.; Cheng, P.; Zaworotko, M. J.; Zhang, Z. Robust Ultramicroporous Metal-Organic Frameworks with Benchmark Affinity for Acetylene. *Angew. Chem., Int. Ed.* **2018**, *57*, 10971−10975.

(25) Lee, J.; Chuah, C. Y.; Kim, J.; Kim, Y.; Ko, N.; Seo, Y.; Kim, K.; Bae, T. H.; Lee, E. Separation of Acetylene from Carbon Dioxide and Ethylene by a Water-Stable Microporous Metal-Organic Framework with Aligned Imidazolium Groups inside the Channels. *Angew. Chem., Int. Ed.* **2018**, *57*, 7869−7873.

(26) Pei, J.; Shao, K.; Wang, J.-X.; Wen, H.-M.; Yang, Y.; Cui, Y.; Krishna, R.; Li, B.; Qian, G. A Chemically Stable Hofmann-Type

Metal-Organic Framework with Sandwich-Like Binding Sites for Benchmark Acetylene Capture. *Adv. Mater.* **2020**, *32*, No. 1908275.
(27) Fu, X.-P.; Wang, Y.-L.; Zhang, X.-F.; Zhang, Z.; He, C.-T.; Liu, Q.-Y. Fluorous Metal-Organic Frameworks with Unique Cage-in-Cage Structures Featuring Fluorophilic Pore Surfaces for Efficient C_2H_2/CO_2 Separation. *CCS Chem.* **2022**, *4*, 3416−3425.
(28) Fu, X.-P.; Wang, Y.-L.; Zhang, X.-F.; Krishna, R.; He, C.-T.; Liu, Q.-Y.; Chen, B. Collaborative Pore Partition and Pore Surface Fluorination within a Metal-Organic Framework for High-Performance C_2H_2/CO_2 separation. *Chem. Eng. J.* **2022**, *432*, No. 134433.
(29) Wang, J.; Zhang, Y.; Su, Y.; Liu, X.; Zhang, P.; Lin, R.-B.; Chen, S.; Deng, Q.; Zeng, Z.; Deng, S.; Chen, B. Fine Pore Engineering in a Series of Isoreticular Metal-Organic Frameworks for Efficient C_2H_2/CO_2 Separation. *Nat. Commun.* **2022**, *13*, No. 200.
(30) Mersmann, A.; Fill, B.; Hartmann, R.; Maurer, S. The Potential of Energy Saving by Gas-Phase Adsorption Processes. *Chem. Eng. Technol.* **2000**, *23*, 937−944.
(31) Shi, Y.; Xie, Y.; Cui, H.; Ye, Y.; Wu, H.; Zhou, W.; Arman, H.; Lin, R.-B.; Chen, B. Highly Selective Adsorption of Carbon Dioxide over Acetylene in an Ultramicroporous Metal-Organic Framework. *Adv. Mater.* **2021**, *33*, No. 2105880.
(32) Li, L.; Wang, J.; Zhang, Z.; Yang, Q.; Yang, Y.; Su, B.; Bao, Z.; Ren, Q. Inverse Adsorption Separation of CO_2/C_2H_2 Mixture in Cyclodextrin-Based Metal-Organic Frameworks. *ACS Appl. Mater. Interfaces* **2019**, *11*, 2543−2550.
(33) Lin, J.-B.; Nguyen, T. T. T.; Vaidhyanathan, R.; Burner, J.; Taylor, J. M.; Durekova, H.; Akhtar, F.; Mah, R. K.; Ghaffari-Nik, O.; Marx, S.; Fylstra, N.; Iremonger, S. S.; Dawson, K. W.; Sarkar, P.; Hovington, P.; Rajendran, A.; Woo, T. K.; Shimizu, G. K. H. A Scalable Metal-Organic Framework as a Durable Physisorbent for Carbon Dioxide Capture. *Science* **2021**, *374*, 1464−1469.
(34) Hu, T.-L.; Wang, H.; Li, B.; Krishna, R.; Wu, H.; Zhou, W.; Zhao, Y.; Han, Y.; Wang, X.; Zhu, W.; Yao, Z.; Xiang, S.; Chen, B. Microporous Metal-Organic Framework with Dual Functionalities for Highly Efficient Removal of Acetylene from Ethylene/Acetylene Mixtures. *Nat. Commun.* **2015**, *6*, No. 7328.
(35) Xie, Y.; Cui, H.; Wu, H.; Lin, R.-B.; Zhou, W.; Chen, B. Electrostatically Driven Selective Adsorption of Carbon Dioxide over Acetylene in an Ultramicroporous Material. *Angew. Chem., Int. Ed.* **2021**, *60*, 9604−9609.
(36) Zhang, Z.; Peh, S. B.; Krishna, R.; Kang, C.; Chai, K.; Wang, Y.; Shi, D.; Zhao, D. Optimal Pore Chemistry in an Ultramicroporous Metal-Organic Framework for Benchmark Inverse CO_2/C_2H_2 Separation. *Angew. Chem., Int. Ed.* **2021**, *60*, 17198−17204.
(37) Qazvini, O. T.; Babarao, R.; Telfer, S. G. Selective Capture of Carbon Dioxide from Hydrocarbons using a Metal-Organic Framework. *Nat. Commun.* **2021**, *12*, No. 197.
(38) Cui, J.; Qiu, Z.; Yang, L.; Zhang, Z.; Cui, X.; Xing, H. Kinetic-Sieving of Carbon Dioxide from Acetylene through a Novel Sulfonic Ultramicroporous Material. *Angew. Chem., Int. Ed.* **2022**, *61*, No. e202208756.
(39) Gu, Y.; Zheng, J.-J.; Otake, K.-i.; Shivanna, M.; Sakaki, S.; Yoshino, H.; Ohba, M.; Kawaguchi, S.; Wang, Y.; Li, F.; Kitagawa, S. Host-Guest Interaction Modulation in Porous Coordination Polymers for Inverse Selective CO_2/C_2H_2 Separation. *Angew. Chem., Int. Ed.* **2021**, *60*, 11688−11694.
(40) Cai, L.-Z.; Yao, Z.-Z.; Lin, S.-J.; Wang, M.-S.; Guo, G.-C. Photoinduced Electron-Transfer (PIET) Strategy for Selective Adsorption of CO_2 over C_2H_2 in a MOF. *Angew. Chem., Int. Ed.* **2021**, *60*, 18223−18230.
(41) Choi, D. S.; Kim, D. W.; Kang, D. W.; Kang, M.; Chae, Y. S.; Hong, C. S. Highly Selective CO_2 Separation from a CO_2/C_2H_2 Mixture using a Diamine-Appended Metal-Organic Framework. *J. Mater. Chem. A* **2021**, *9*, 21424−21428.
(42) Ma, D.; li, Z.; Zhu, J.; Zhou, Y.; Chen, L.; Mai, X.; Liufu, M.; Wu, Y.; Li, Y. Inverse and Highly Selective Separation of CO_2/C_2H_2 on a Thulium-Organic Framework. *J.Mater. Chem. A* **2020**, *8*, 11933−11937.
(43) Li, X.-Y.; Song, Y.; Zhang, C.-X.; Zhao, C.-X.; He, C. Inverse CO_2/C_2H_2 Separation in a Pillared-Layer Framework Featuring a Chlorine-Modified Channel by Quadrupole-Moment Sieving. *Sep. Purif. Technol.* **2021**, *279*, No. 119608.
(44) Cui, H.; Xie, Y.; Ye, Y.; Shi, Y.; Liang, B.; Chen, B. An Ultramicroporous Metal-Organic Framework with Record High Selectivity for Inverse CO_2/C_2H_2 Separation. *Bull. Chem. Soc. Jpn.* **2021**, *94*, 2698−2701.
(45) Krishna, R. Methodologies for Evaluation of Metal-Organic Frameworks in Separation Applications. *RSC Adv.* **2015**, *5*, 52269−52295.
(46) Krishna, R. Synergistic and Antisynergistic Intracrystalline Diffusional Influences on Mixture Separations in Fixed Bed Adsorbers. *Precis. Chem.* **2023**, *1*, 83−93.
(47) Krishna, R. Screening Metal-Organic Frameworks for Mixture Separations in Fixed-Bed Adsorbers using a Combined Selectivity/Capacity Metric. *RSC Adv.* **2017**, *7*, 35724−35737.
(48) Krishna, R. Metrics for Evaluation and Screening of Metal-Organic Frameworks for Applications in Mixture Separations. *ACS Omega* **2020**, *5*, 16987−17004.
(49) Ma, B.; Li, D.; Zhu, Q.; Li, Y.; Ueda, W.; Zhang, Z. A Zeolitic Octahedral Metal Oxide with Ultra-Microporosity for Inverse CO_2/C_2H_2 Separation at High Temperature and Humidity. *Angew. Chem., Int. Ed.* **2022**, *61*, No. e202209121.

https://doi.org/10.1021/jacs.3c03265
J. Am. Chem. Soc. 2023, 145, 13901−13911

Supporting Information

Immobilization of Polar Group into an Ultramicroporous Metal-Organic Framework Enabling Benchmark Inverse Selective CO_2/C_2H_2 Separation with Record C_2H_2 Production

Shan-Qing Yang,[a] Rajamani Krishna,[b] Hongwei, Chen,[c] Libo Li,[c] Lei Zhou,[a] Yi-Feng An,[a] Fei-Yang Zhang,[a] Qiang Zhang,[a] Ying-Hui Zhang,[a] Wei Li,[a] Tong-Liang Hu,[a]* Xian-He Bu[a]

[a] School of Materials Science and Engineering, National Institute for Advanced Materials, Nankai University, Tianjin 300350, China. E-mail: tlhu@nankai.edu.cn (T.-L. Hu)

[b] Van 't Hoff Institute for Molecular Sciences, University of Amsterdam, Science Park 904, 1098 XH Amsterdam, The Netherlands.

[c] College of Chemistry and Chemical Engineering, Shanxi Key Laboratory of Gas Energy Efficient and Clean Utilization, Taiyuan University of Technology, Taiyuan, 030024, Shanxi, China.

Experimental section

Materials and Methods

All raw reagents and chemicals were purchased from commercial providers and used directly without further purification.

The powder X-ray diffraction (PXRD) patterns were collected on the Rigaku Miniflex 600 at 40 kV and 15 mA with a scan rate of 5.0 ° min^{-1} using Cu Kα (λ = 1.5418 Å) radiation in the air atmosphere, scanning the 2θ range of 3-50° with a step size of 0.02 °. The thermogravimetric analysis (TGA) was performed on a Rigaku standard thermogravimetry-differential thermal analysis (TG-DTA) analyzer from room temperature to 800 °C under Argon atmosphere with a heating rate of 10 °C min^{-1}, using an empty and clean Al_2O_3 crucible as a reference. In situ variable temperature PXRD (VT-PXRD) patterns were also collected on a Rigaku Miniflex 600 at 40 kV and 15 mA with a scan rate of 8.0 ° min^{-1} using Cu Kα (λ = 1.5418 Å) radiation in the air atmosphere, scanning the 2θ range of 3-40° with a step size of 0.02 °.

Synthesis of Zn-ox-trz and Zn-ox-mtz

Synthesis of Zn-ox-mtz ($Zn_2(ox)(mtz)_2 \cdot 2H_2O$). A mixture of $ZnCO_3$ (0.125 g), oxalic acid (0.09 g), 3-methyl-1H-1,2,4-triazole (0.415 g), H_2O (4 mL) and BuOH (2 mL) was placed in a 20 ml Teflon autoclave, which was stirred for 30 minutes at room temperature and then was heated in a convection oven at 180 °C for 3 days.

Synthesis of Zn-ox-trz. Zn-ox-trz was prepared according to the previously reported method with some modifications.[1] The mixture of zinc oxalate (0.66 g) 1,2,4-triazole (0.5 g) was added into 6.6 mL methanol in a 20 mL Teflon autoclave, which was stirred

for 30 minutes at room temperature and then was heated in a convection oven at 180 °C for 2 days.

Single crystal X-ray diffraction analysis

The single crystal X-ray diffraction data of **Zn-ox-mtz** were collected at 100 K, via Rigaku XtaLAB Pro MM007HF DW diffractometer with Cu-Ka radiation (2λ = 1.54184 Å). The structure was solved and refined using Olex2 software with the SHELXT and SHELXL program, respectively. The crystal details are listed in Table S3, and the crystallographic data of **Zn-ox-mtz** can be obtained freely from the Cambridge Crystallographic Data Centre (CCDC: 2248518).

Gas sorption measurements

CO_2 and C_2H_2 sorption isotherms were collected on the BSD-PM2 instrument. N_2 (99.9999%), C_2H_2 (99.9%), CO_2 (99.99%), He (99.999%) were purchased from Liquid Air (China). Prior to the gas sorption analysis, the samples were washed with methanol several times and activated under dynamic vacuum overnight at 100 °C. The precise control of 298, 313, and 333 K were implemented by the BSD 3H-2000 of Beishide Instrument Technology**,** which contains a cycle system of water. The sample was degassed at 60 ºC under high vacuum for 1 h to regenerate at every interval of two independent sorption isotherms.

Fitting of experimental data on pure component isotherms

The unary isotherm data for CO_2, measured at three different temperatures 298 K, 313 K, and 333 K in Zn-ox-trz and **Zn-ox-mtz** were fitted with excellent accuracy using the dual-site Langmuir model, where we distinguish two distinct adsorption sites A and B:

$$q = \frac{q_{sat,A} b_A p}{1 + b_A p} + \frac{q_{sat,B} b_B p}{1 + b_B p} \quad \text{(S1)}$$

In eq (S1), the Langmuir parameters b_A, b_B are both temperatures dependent.

$$b_A = b_{A0} \exp\left(\frac{E_A}{RT}\right); \quad b_b = b_{B0} \exp\left(\frac{E_B}{RT}\right) \quad \text{(S2)}$$

In eq (S2), E_A, E_B are the energy parameters associated with sites A, and B, respectively.

The fit parameters are provided in Table S1 for the two MOFs.

The unary isotherm data for C_2H_2, measured at three different temperatures 298 K, 313 K, and 333 K in Zn-ox-trz and **Zn-ox-mtz**, could be fitted with the 1-site Langmuir-Freundlich model:

$$q = \frac{q_{sat} b p^{\nu}}{1 + b p^{\nu}} \quad \text{(S3)}$$

In eq (S3), the Langmuir-Freundlich parameter b is temperature dependent.

$$b = b_0 \exp\left(\frac{E}{RT}\right) \quad \text{(S4)}$$

In eq (S4), E is the energy parameter. The fit parameters are provided in

Table **S2** for the two MOFs.

Isosteric heat of adsorption

The isosteric heat of adsorption, Q_{st}, is defined as

$$Q_{st} = -RT^2 \left(\frac{\partial \ln p}{\partial T}\right)_q \quad \text{(S5)}$$

where the derivative in the right member of eq (S5) is determined at constant adsorbate loading, q. The derivative was determined by analytic differentiation of the combination

of eq (S1), eq (S2), and eq (S5) for the dual-site Langmuir fits. For the 1-site Langmuir-Freundlich fits, the isosteric heat of adsorption, Q_{st}, was determined by analytic differentiation of the combination of eq (S3), eq (S4), and eq (S5).

IAST calculations

For screening MOFs for separation of binary mixtures of components 1 and 2, the adsorption selectivity, S_{ads}, is defined by

$$S_{ads} = \frac{q_1/q_2}{y_{10}/y_{20}} \tag{S6}$$

In eq (S6), y_{10}, y_{20} are the mole fractions of the bulk gas phase mixture.

The 50/50 CO_2 (1)/C_2H_2 (2) mixture separations are envisaged to be carried out in fixed bed adsorbers. In such devices, the separations are dictated by a combination of adsorption selectivity and uptake capacity. Using the shock wave model for fixed bed adsorbers, Krishna[2-3] has suggested that the appropriate metric is the separation potential, Δq. The appropriate expression describing the productivity of pure C_2H_2 in the adsorption phase of fixed-bed operations is

$$\Delta q = q_1 \frac{y_{20}}{y_{10}} - q_2 \tag{S7}$$

In eq (S7) $y_{10} = y_{20} = 0.5$ is the mole fractions of the feed mixture during the adsorption cycle. In the derivation of eq (S7), it is assumed that the concentration "fronts" traversed the column in the form of shock waves during the desorption cycle. The molar loadings q_1, q_2 of the two components are determined using the Ideal Adsorbed Solution Theory (IAST) of Myers and Prausnitz using the unary isotherm fits

as data inputs.[4] The physical significance of Δq_1 is the maximum productivity of pure C_2H_2 that is achievable in PSA operations.

Grand canonical Monte Carlo simulations

The GCMC simulations were carried out for the adsorption of C_2H_2 and CO_2 in Zn-MOFs using Sorption Tools in Materials Studio package. The skeleton of Zn-MOFs and gas molecules were regarded as rigid bodies. The optimal adsorption sites were simulated under 298 K and 1.0 bar by the fixed loading task and Metropolis method. The atomic partial charges of the host skeleton of Zn-MOFs and all gas molecules were obtained from QEq method. The equilibration steps and the production steps were set to 5.0×10^6 and 1.0×10^7, respectively. The gas-skeleton interaction and the gas-gas interaction were characterized by the standard universal force field (UFF). The cut-off radius used for the Lennard-Jones interactions is 15.5 Å and the long-range electrostatic interactions were considered by the Ewald summation method.

Density-functional theory calculations

All density functional theory (DFT) calculations were performed using the Vienna Ab initio Simulation Package (VASP)[5,6] at the level of generalized gradient approximation (GGA) using Perdew-Burke-Ernzerhof (PBE) exchange-correlation functional.[7] Projector-augmented wave (PAW) potentials were used to describe the effective cores.[8,9] The valence electrons of all atoms were expanded in a plane wave basis set with a cutoff energy of 400 eV. The atomic structures were relaxed using either the conjugate gradient algorithm or the quasi-Newton scheme as implemented in the VASP code until the forces were less than 0.05 eV/Å for all unconstrained atoms, and the

energy convergence criteria for all self-consistent field calculations were set as 10^{-5} eV. The Brillouin zone integration was sampled with 2 × 2 × 2 Monkhorst-Pack mesh k-points.[10]

The adsorption energy was defined as

$$E_{ads} = E(MOF/M) - E(MOF) - E(M) \quad (S8)$$

where the *E*(MOF/M), *E*(MOF) and *E*(M) represent the total energies of MOF with the adsorbate, the optimized MOF structure and the isolated gas molecules, respectively.

Zn-ox-trz**:**

$E_{ads}(2CO_2)$ = -0.3 eV = -28.95 kJ mol^{-1}

$E_{ads}(CO_2)$ = -0.15 eV = -14.47 kJ mol^{-1}

$E_{ads}(2C_2H_2)$ = -0.2 eV = -19.30 kJ mol^{-1}

$E_{ads}(C_2H_2)$ = -0.1 eV = -9.65 kJ mol^{-1}

Zn-ox-mtz:

$E_{ads}(CO_2)$ = -0.1 eV = -9.65 kJ mol^{-1}

$E_{ads}(C_2H_2)$ = 0.3 eV = 28.95 kJ mol^{-1}

Breakthrough experiments

Breakthrough experiments of **Zn-ox-mtz** and Zn-ox-trz for the equimolar CO_2/C_2H_2 mixtures were performed on a homemade dynamic separation device (CO_2/C_2H_2, 50/50, v/v, mass flow rate = 2 mL min^{-1}). Prior to the breakthrough experiment, the as-synthesized sample was firstly activated at 373 K for 12 h at the activation station, after activation, the sample was packed into a self-made adsorption column stain steel column and further flushing the packed column with helium gas for 1 h under room

temperature at a flow rate of 10 mL min^{-1}. The outlet gas from the column was monitored using gas chromatography (Agilent GC 490).

Transient breakthrough simulations

Transient breakthrough simulations were carried out for the same set of operating conditions as in the experimental data sets, using the methodology described in earlier publications.[2,3,11,12]

We summarize below the simulation methodology used to perform transient breakthrough calculations for fixed bed adsorbers; see schematics in Figure S20 and Figure S21. For an *n*-component gas mixtures in plug flow through a fixed bed maintained under isothermal conditions, the molar concentrations in the gas phase at any position and instant of time are obtained by solving the following set of partial differential equations for each of the species *i* in the gas mixture.

$$\frac{\partial c_i(t,z)}{\partial t}+\frac{\partial\left(v(t,z)c_i(t,z)\right)}{\partial z}+\frac{\left(1-\varepsilon\right)}{\varepsilon}\rho\frac{\partial\bar{q}_i(t,z)}{\partial t}=0;\quad i=1,2,...n \qquad \text{(S9)}$$

In eq (S9), t is the time, z is the distance along the adsorber, ρ is the framework density, ε is the bed voidage, v is the interstitial gas velocity, and $\bar{q}_i(t,z)$ is the *spatially averaged* molar loading within the crystallites of radius r_c, monitored at position z, and at time t. The time t = 0, corresponds to the time at which the feed mixture is injected at the inlet to the fixed bed.

The radial distribution of molar loadings, q_i, within a spherical MOF crystallite, of radius r_c, is obtained from a solution of a set of differential equations describing the uptake.

$$\rho \frac{\partial q_i(r,t)}{\partial t} = -\frac{1}{r^2}\frac{\partial}{\partial r}\left(r^2 N_i\right) \tag{S10}$$

The intra-crystalline fluxes N_i in eq (S10) are related to gradients in the chemical potential gradients by the Maxwell-Stefan equations.[11,12]

$$N_i = -\rho Đ_i \frac{q_i}{RT}\frac{\partial \mu_i}{\partial r} \tag{S11}$$

In eqs (S10) and (S11), R is the gas constant, T is the temperature, ρ represents the framework density of the microporous crystalline material, r is the radial distance coordinate, and the component loadings q_i are defined in terms of moles per kg of framework. The $Đ_i$ characterize and quantify the interaction between species i and pore walls. The M-S diffusivity $Đ_i$ equals the corresponding diffusivity for a unary system, determined at the same pore occupancy.

At any time, t, during the transient approach to thermodynamic equilibrium, the spatial-averaged component loading within the crystallites of radius r_c is calculated using.

$$\bar{q}_i(t) = \frac{3}{r_c^3}\int_0^{r_c} q_i(r,t) r^2 dr \tag{S12}$$

Summing eq (S12) over all n species in the mixture allows calculation of the *total average* molar loading of the mixture within the crystallite.

$$\bar{q}_t(t,z) = \sum_{i=1}^{n} \bar{q}_i(t,z) \tag{S13}$$

The term $\frac{\partial \bar{q}_i(t,z)}{\partial t}$ in eq (S9) is determined by solving the set of eqs (S10), (S11), (S12), and (S13). At any time t, and position z, the component loadings at the outer surface of the particle $q_i(r_c,t,z)$ is in equilibrium with the bulk phase gas mixture with partial pressures $p_i(t,z)$ in the bulk gas mixture. the component loadings at the surface

of the crystallites $q_i(r_c,t,z)$ are calculated using the Ideal Adsorbed Solution Theory (IAST)

The interstitial gas velocity is related to the *superficial* gas velocity by

$$v = \frac{u}{\varepsilon} \tag{S14}$$

At time, t = 0, the inlet to the adsorber, z = 0, is subjected to a step input of the n-component gas mixture and this step input is maintained till the end of the adsorption cycle when steady-state conditions are reached.

$$t \geq 0; \quad p_i(0,t) = p_{i0}; \quad u(0,t) = u_0 \tag{S15}$$

where $u_0 = v\varepsilon$ is the superficial gas velocity at the inlet to the adsorber.

The adsorber tube is divided into 100 slices, and each spherical crystallite was discretized into 20-50 equi-volume slices. The results thus obtained were confirmed to be of adequate accuracy. Combination of the discretized partial differential equations (PDEs) along with the algebraic equations describing mixture adsorption equilibrium (IAST), results in a set of differential-algebraic equations (DAEs), which are solved using BESIRK.[11,12] BESIRK is a sparse matrix solver, based on the semi-implicit Runge-Kutta method originally developed by Michelsen, and extended with the Bulirsch-Stoer extrapolation method.[11,12] Use of BESIRK improves the numerical solution efficiency in solving the set of DAEs. The evaluation of the sparse Jacobian required in the numerical algorithm is largely based on analytic expressions.

We describe below how we compare experimental data on transient breakthroughs with breakthrough simulations using the methodology outlined in the foregoing section.

The following data are available for the experimental breakthroughs.

Inside diameter of tube of diameter: d = 10 mm.

Effective length of packed column: L.

The mass of the crystallites of Zn-ox-mtz in the packed tube: m_{ads} = 1.8867 g.

The crystal framework density ρ kg m^{-3}.

Total pressure, p_t = 1 bar and temperature, T = 298 K at which the experiments are conducted.

Composition of entering gas phase mixture = 50/50.

The total flow rate of the gas mixture at the entrance to the tube Q_0 = 2 mL min^{-1}.

We calculate $(1-\varepsilon)=\frac{m_{ads}/\rho}{\pi d^2 L/4}$ and $\varepsilon=1-\frac{m_{ads}/\rho}{\pi d^2 L/4}$.

The superficial gas velocity at the inlet to the adsorber $u=\frac{Q_0}{\pi d^2/4}$.

The interstitial velocity $v=\frac{u}{\varepsilon}$.

For Zn-ox-trz and Zn-ox-mtz, the diffusional limitations are described by choosing the diffusional time constant $\frac{Đ_i}{r_c^2}$ = 1×10^{-4} s^{-1} for both CO_2, and C_2H_2. The chosen diffusivities allow good match with experiments.

Separation factor and gas purity productivity

The breakthrough selectivity (separation factor) was defined,[13] the values were calculated by the equation:

$$S_b = \frac{q_i/y_i}{q_j/y_j} \quad \text{(S17)}$$

where q_i is the equilibrium adsorption capacity of component i, q_j is the equilibrium adsorption capacity of component j; and y_i and y_j are the molar fractions of component i and j in gas phase, respectively.

The equilibrium adsorption capacity of gas i (q_i) and j (q_j) (mmol g^{-1}) were calculated from the breakthrough curve by the equation:

$$q_i = \frac{f_i\,(t_1 - t_0) - f_i \int_{t_0}^{t_1} F_i(t)dt}{22.4 \times m} \quad \text{(S18)}$$

$$q_j = \frac{f_j\,(t_1 - t_0) - f_j \int_{t_0}^{t_1} F_j(t)dt}{22.4 \times m} \quad \text{(S19)}$$

The calculation method of the C_2H_2 purity (c) is as follows

$$c = \frac{q_{C_2H_2}}{q_{C_2H_2} + q_{CO_2}} \quad \text{(S20)}$$

The gas breakthrough gas amount (q_i) (mmol g^{-1}) was calculated by integrating the breakthrough curve $F_i(t)$ as following equation:

$$q_i = \frac{f_i \int_0^{t_1} F_i(t)dt}{22.4 \times m} \quad \text{(S21)}$$

Where the m represents the adsorbent mass, f_i is the flow rate of gas i (mL min^{-1}); $F_i(t)$ is the function of the breakthrough curve of component i.

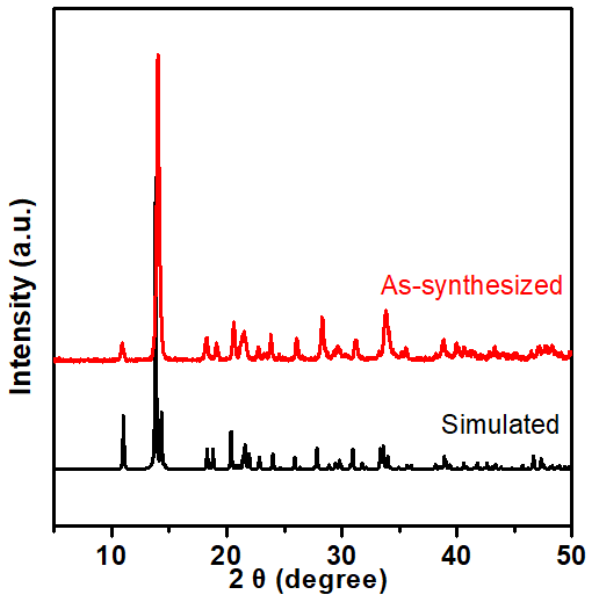

Figure S1. PXRD patterns of Zn-ox-trz. The experimental result of as-synthesized sample and the simulation one from single crystal X-ray diffraction data.

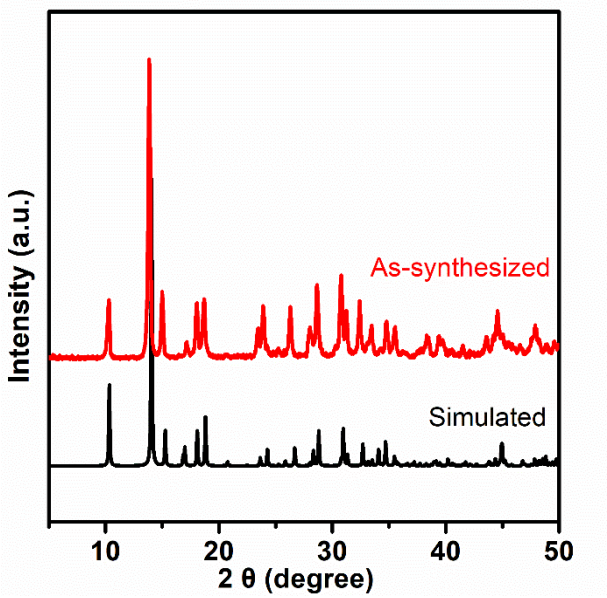

Figure S2. PXRD patterns of **Zn-ox-mtz**. The experimental result of as-synthesized sample and the simulation one from single crystal X-ray diffraction data.

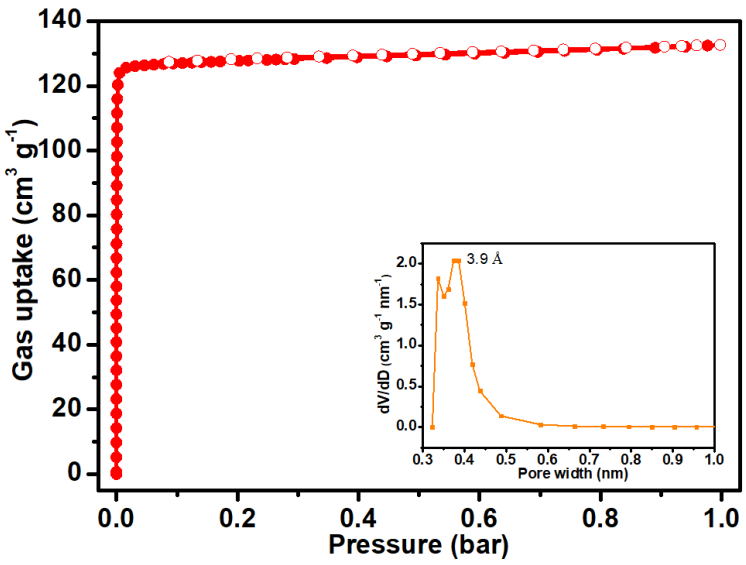

Figure S3. CO_2 sorption isotherms at 195 K on Zn-ox-trz.

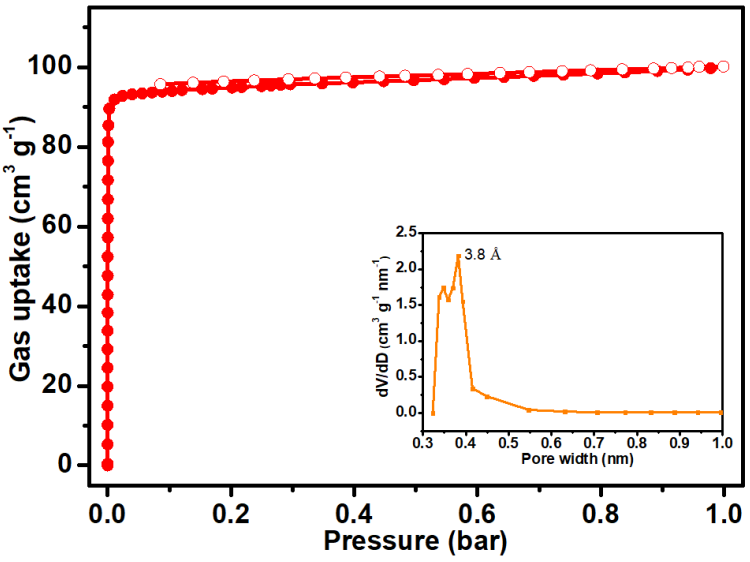

Figure S4. CO_2 sorption isotherms at 195 K on **Zn-ox-mtz**.

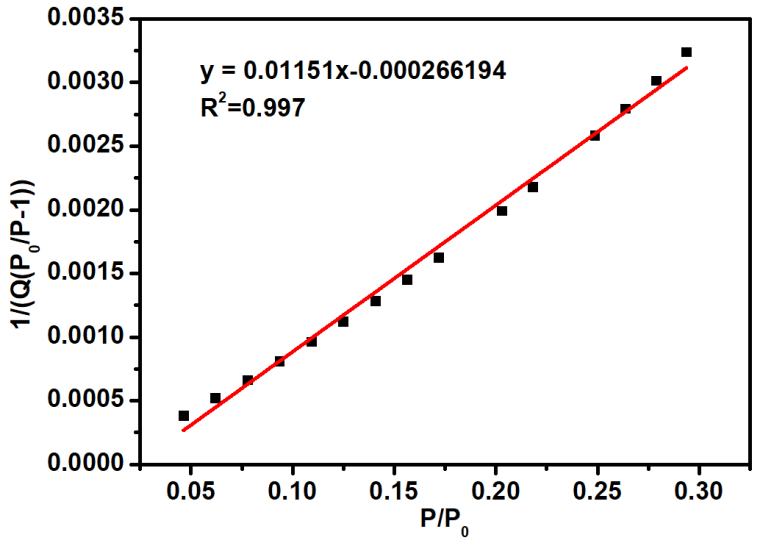

Figure S5. BET surface area plots of Zn-ox-trz.

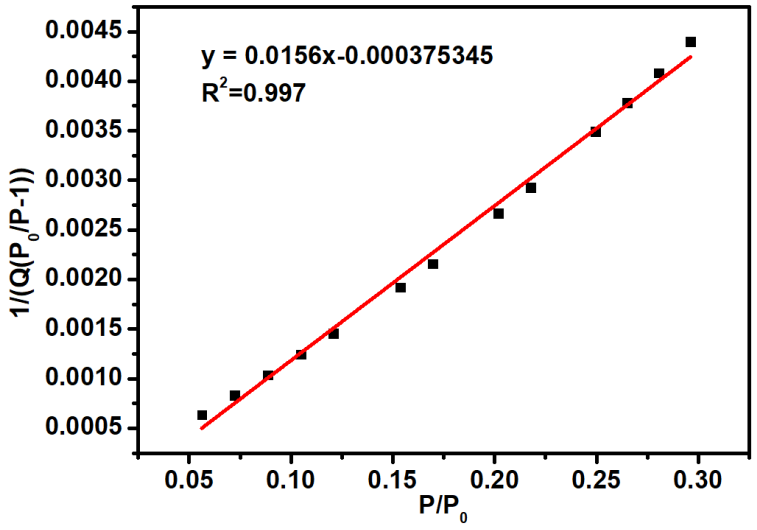

Figure S6. BET surface area plots of **Zn-ox-mtz**.

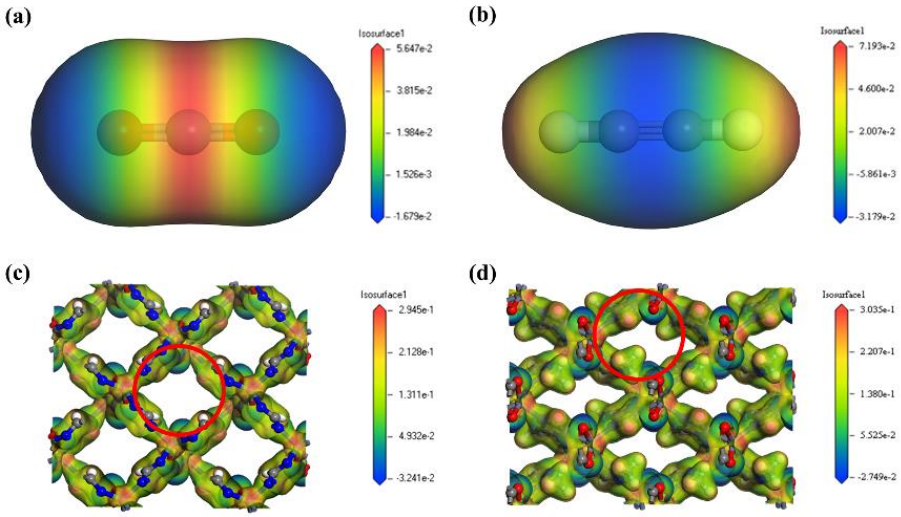

Figure S7. The electrostatic potential of gas molecules: (a) CO_2 molecule, (b) C_2H_2 molecule; and pore surfaces: (c) Zn-ox-trz framework, (d) **Zn-ox-mtz** framework.

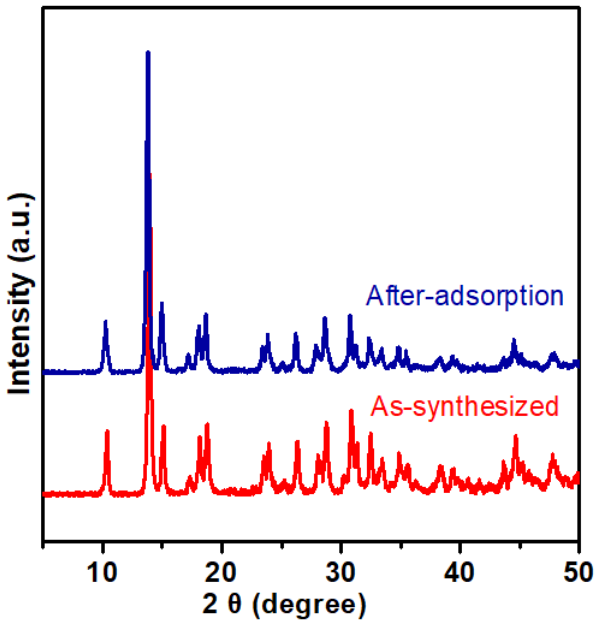

Figure S8. PXRD patterns of **Zn-ox-mtz**. The experimental result of as-synthesized sample and the sample of after-sorption experiments.

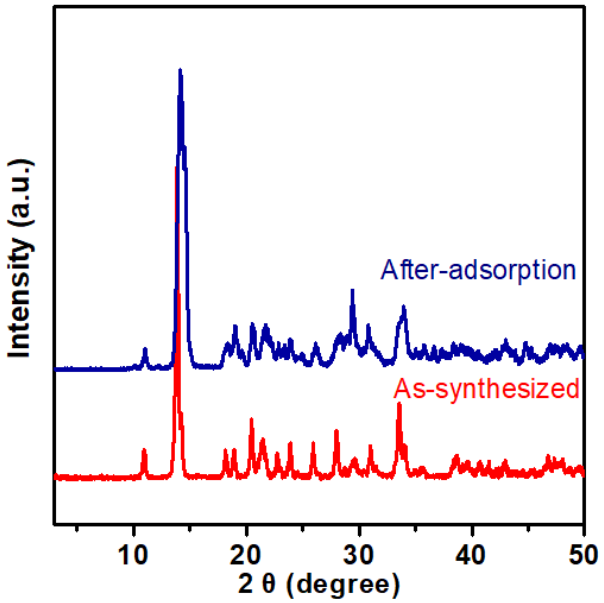

Figure S9. PXRD patterns of Zn-ox-trz. The experimental result of as-synthesized sample and the sample of after-sorption experiments.

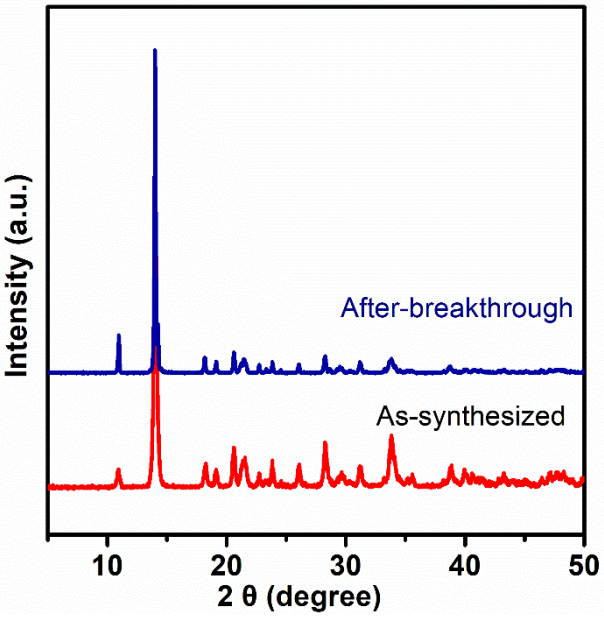

Figure S10. PXRD patterns of Zn-ox-trz. The experimental result of as-synthesized sample and the sample of after-breakthrough experiments.

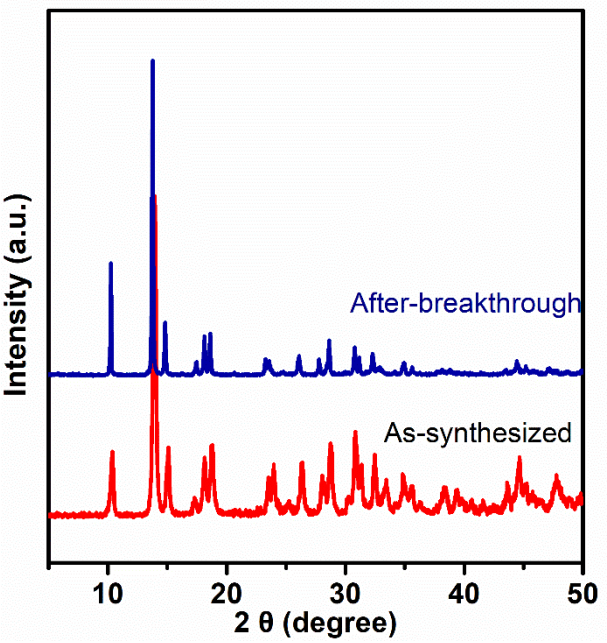

Figure S11. PXRD patterns of **Zn-ox-mtz**. The experimental result of as-synthesized sample and sample of after-breakthrough experiments.

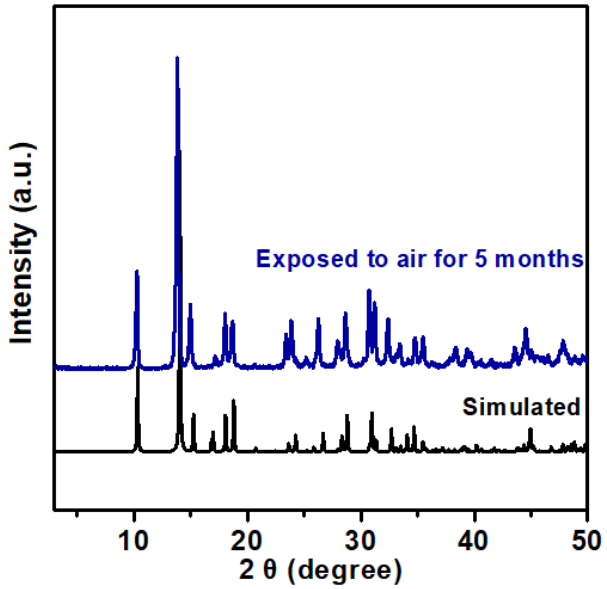

Figure S12. PXRD patterns of **Zn-ox-mtz**. The experimental result of sample exposed to air for 5 months and the simulation one from single crystal X-ray diffraction data.

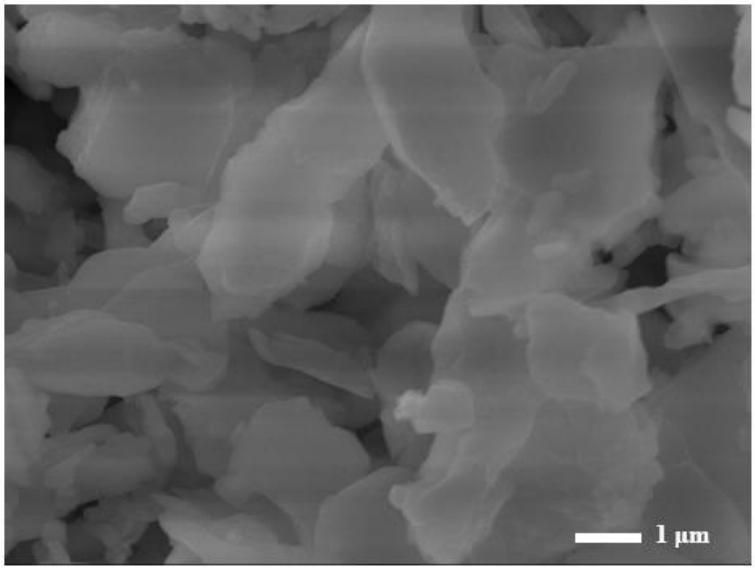

Figure S13. The SEM image of **Zn-ox-mtz**.

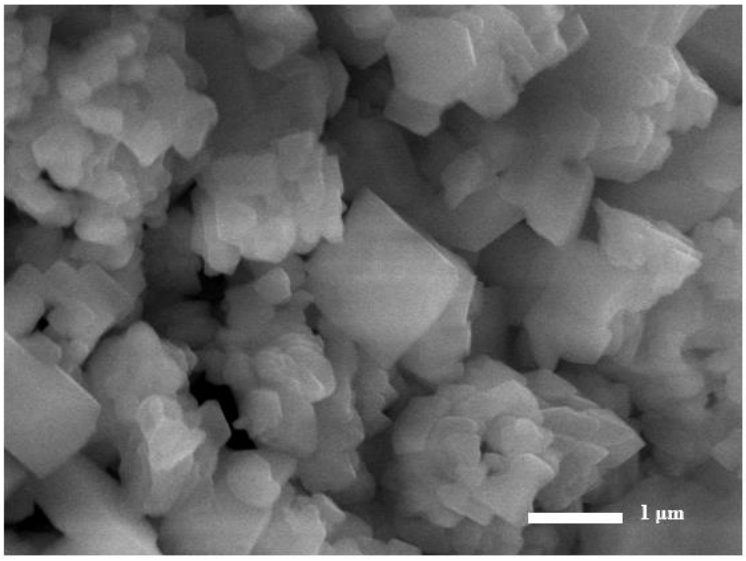

Figure S14. The SEM image of Zn-ox-trz.

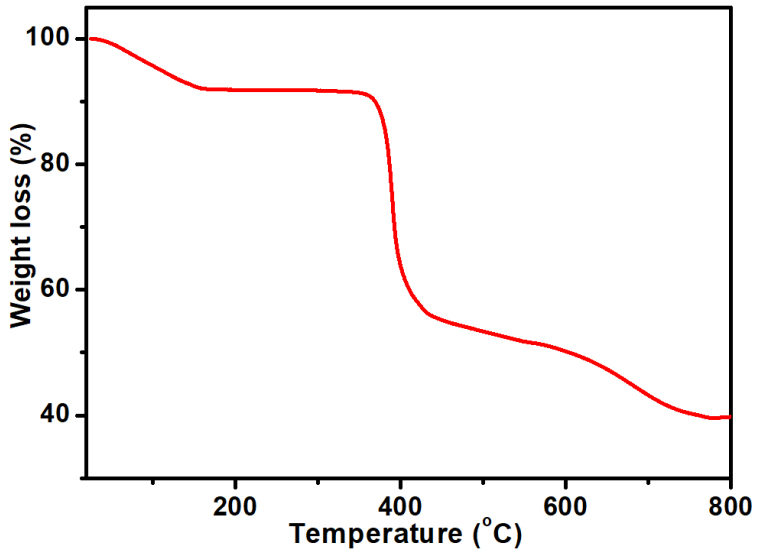

Figure S15. TG curve of **Zn-ox-mtz** under argon atmosphere.

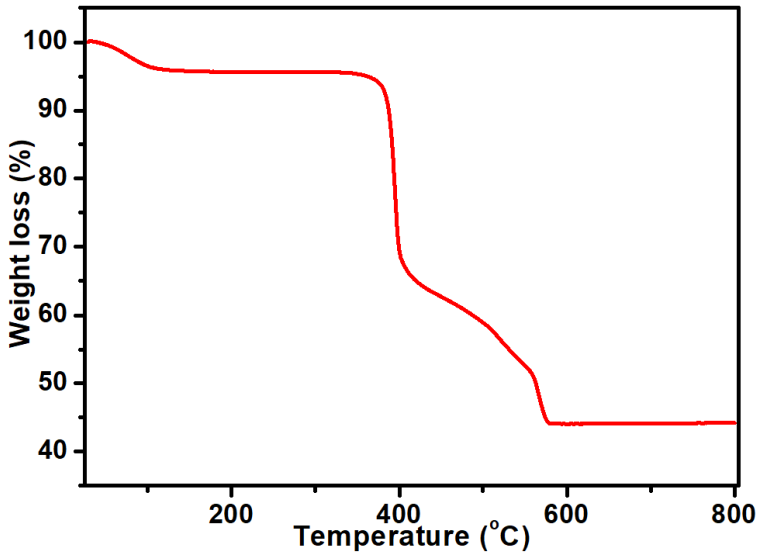

Figure S16. TG curve of Zn-ox-trz under argon atmosphere.

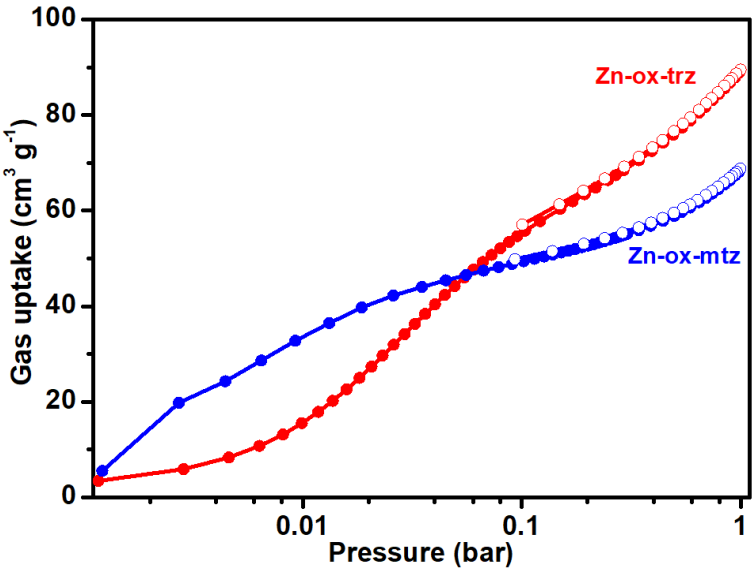

Figure S17. The comparison of CO_2 uptake profiles between Zn-ox-trz and **Zn-ox-mtz** at 298 K and 1.0 bar.

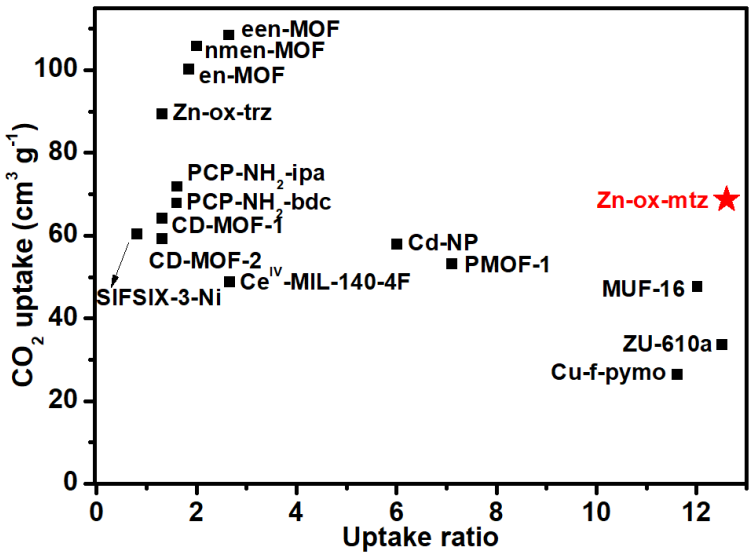

Figure S18. Comparison of CO_2/C_2H_2 uptake ratio and CO_2 uptake with representative CO_2-selective adsorbents at ambient conditions.

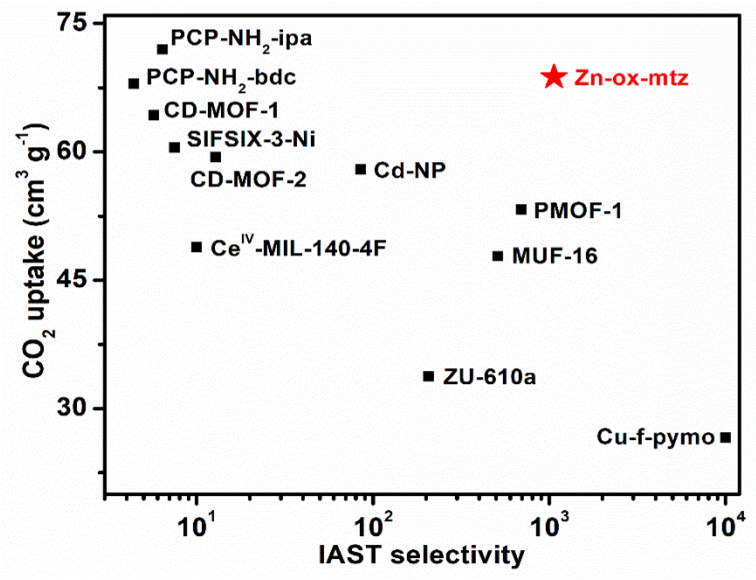

Figure S19. Comparison of equimolar CO_2/C_2H_2 selectivity and CO_2 uptake with representative CO_2-selective adsorbents at ambient conditions.

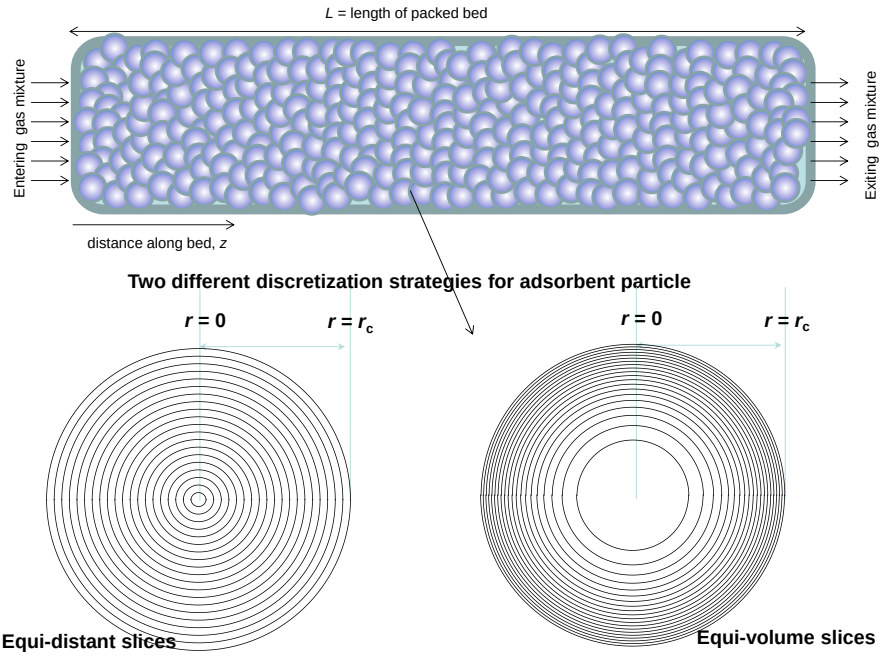

Figure S20. Two different discretization schemes for a single spherical crystallite.

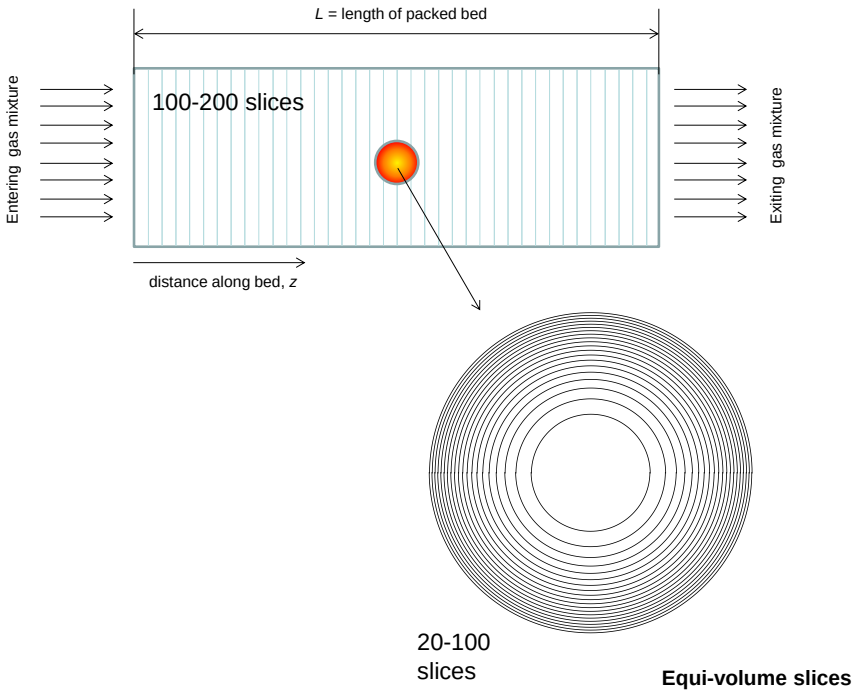

Figure S21. Discretization scheme for fixed bed adsorber.

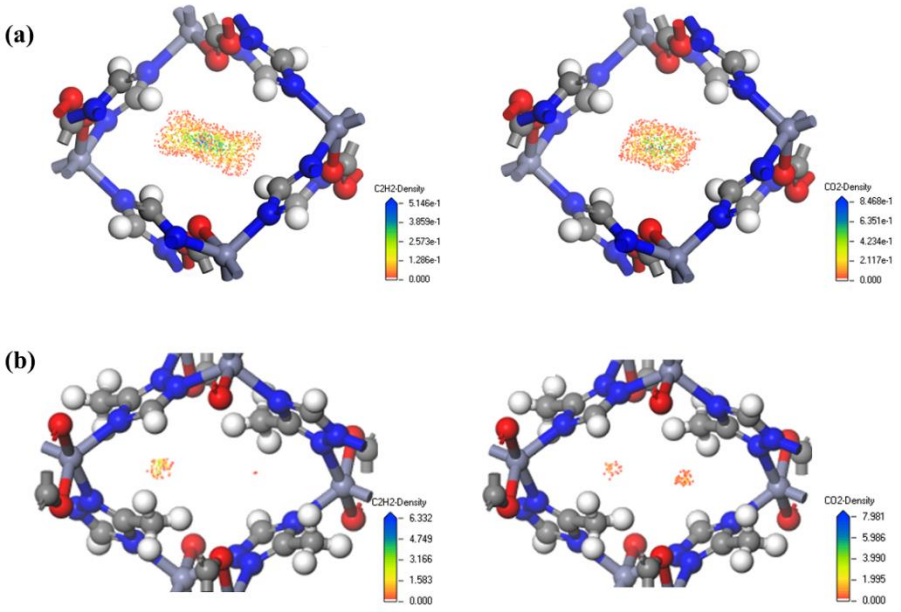

Figure S22. Adsorption density distribution calculated by GCMC simulation at 298 K and 1.0 bar for C_2H_2 and CO_2 in (a) Zn-ox-trz and (b) **Zn-ox-mtz**.

Table S1. Dual-site Langmuir fits for CO_2 in Zn-ox-trz and **Zn-ox-mtz**.

	Site A			Site B		
	$\frac{q_{A,sat}}{\text{mol/kg}}$	$\frac{b_{A0}}{\text{Pa}^{-1}}$	$\frac{E_A}{\text{kJ mol}^{-1}}$	$\frac{q_{B,sat}}{\text{mol/kg}}$	$\frac{b_{B0}}{\text{Pa}^{-1}}$	$\frac{E_B}{\text{kJ mol}^{-1}}$
Zn-ox-trz	3.2	6.150×10^{-11}	38	3	4.766×10^{-14}	45
Zn-ox-mtz	2.3	4.245×10^{-11}	43	3	3.472×10^{-15}	51

Table S2. 1-site Langmuir-Freundlich fits for C_2H_2 in Zn-ox-trz and **Zn-ox-mtz**.

	$\frac{q_{sat}}{\text{mol kg}^{-1}}$	$\frac{b_0}{\text{Pa}^{-\nu}}$	$\frac{E}{\text{kJ mol}^{-1}}$	ν
Zn-ox-trz	3.0	6.560×10^{-15}	52.6	1.37
Zn-ox-mtz	3.5	1.375×10^{-6}	4.5	0.78

Table S3. Crystallographic parameters and refinement details of **Zn-ox-mtz**.

	Zn-ox-mtz
Formula	$C_4H_6N_3O_3Zn$
*M*r (g mol^{-1})	209.49
Crystal system	monoclinic
Space group	$P2_1/c$
a (Å)	8.6166(2)
b (Å)	7.8948(1)
c (Å)	10.5066(2)
α (°)	90
β (°)	96.968(2)
γ (°)	90
V (Å^3)	709.45(2)
Z	4
D_c (g cm^{-3})	1.961
F (000)	420.0
μ (mm^{-1})	4.558
GOF on F^2	1.149
R_1, wR_2 [$I>2\sigma(I)$][a]	0.0387, 0.1001
R_1, wR_2 [all data][b]	0.0442, 0.1018

[a] $R_1 = \sum ||F_o| - |F_c|| / \sum |F_o|$. [b] $wR_2 = \{\sum[w(F_o^2 - F_c^2)^2] / \sum w(F_o^2)^2\}^{1/2}$

Table S4. Summary of adsorption and separation metrics of CO_2-selective materials reported in the literatures at 1 bar and room temperature.[a]

Materials	CO_2 ($cm^3\ g^{-1}$/ $cm^3\ cm^{-3}$)	C_2H_2 ($cm^3\ g^{-1}$/ $cm^3\ cm^{-3}$)	Uptake ratio	IAST	Ref.
Mn(bdc)(dpe)	46.8/64.7	7.4/10.2	6.3	8.8	14
Co(HL^{dc})[b]	239.5/320	140/187	1.7	1.7	15
SIFSIX-3-Ni	60.5/98.4	73.9/120.2	0.8	7.5	16
CD-MOF-1	64.3/-	49.9/-	1.3	5.7	17
CD-MOF-2	59.4/-	45.5/-	1.3	12.8	17
MUF-16	47.8/74.7	4.0/6.3	12	510	18
Cd-NP	58.0/109.4	9.7/18.3	6.0	85	19
PCP-NH_2-ipa	72.0/93.6	43.4/56.4	1.6	6.4	20
PCP-NH_2-bdc	68.0/86.2	42.7/54.0	1.59	4.4	20
Ce(IV)-MIL-1404F	48.9/110.3	18.3/41.4	2.65	~10	21
Cu-F-pymo	26.6/51.5	2.3/4.5	11.6	$>10^5$	22
Tm_2(OH-bdc)$_2$(μ_3-OH)$_2$(H_2O)$_2$	130.6/155.5	47.0/56.0	2.8	18.2	23
Zn(atz) (BDC-Cl_4)$_{0.5}$	34.5/56.8	17.9/29.5	1.9	2.4	24
PMOF-1[c]	53.3/79.6	7.5/11.2	7.1	694	25
ZU-610a	33.8/51.7	2.7/4.1	12.5	207	26
Y-bptc	55.0/73.1	26.2/36.5	2.1	4.1	27
en-MOF	100.352/-	54.432/-	1.8	-	28
nmen-MOF	96.32/-	53.312/-	2.0	-	28

een-MOF	108.64/-	41.22/-	2.6	-	28
Zn-ox-trz	89.49/157.8	67.9/119.6	1.3	1.9	This work
Zn-ox-mtz	68.8/123.3	5.5/9.9	12.6	1064.9	This work

Note:

[a] At the proof stage of this article, we found that the recently published $Al(HCOO)_3$, ALF, had higher CO_2/C_2H_2 inverse selectivity and C_2H_2 production.[29]

[b] data collected at 195 K.

[c] data collected at 273 K.

Reference

(1) Lin, J.-B.; Nguyen, T. T. T.; Vaidhyanathan, R.; Burner, J.; Taylor, J. M.; Durekova, H.; Akhtar, F.; Mah, R. K.; Ghaffari-Nik, O.; Marx, S.; Fylstra, N.; Iremonger, S. S.; Dawson, K. W.; Sarkar, P.; Hovington, P.; Rajendran, A.; Woo, T. K.; Shimizu, G. K. H., A Scalable Metal-Organic Framework as a Durable Physisorbent for Carbon Dioxide Capture. *Science* **2021**, *374*, 1464-1469.

(2) Krishna, R., Screening Metal-Organic Frameworks for Mixture Separations in Fixed-Bed Adsorbers using a Combined Selectivity/Capacity Metric. *RSC Adv.* **2017**, *7*, 35724-35737.

(3) Krishna, R., Metrics for Evaluation and Screening of Metal-Organic Frameworks for Applications in Mixture Separations. *ACS Omega* **2020**, *5*, 16987-17004.

(4) Myers, A. L.; Prausnitz, J. M., Thermodynamics of Mixed Gas Adsorption. *AIChE. J.* **1965**, *11*, 121-127.

(5) Kresse, G.; Furthmüller, J., Efficient Iterative Schemes for ab initio Total-Energy calculations Using a Plane-Wave Basis Set. *Phys. Rev. B* **1996**, *54*, 11169-11186.

(6) Kresse, G.; Furthmüller, J., Efficiency of ab-initio Total Energy Calculations for Metals and Semiconductors Using a Plane-Wave Basis Set. *Comp. Mater. Sci.* **1996**, *6*, 15-50.

(7) Perdew, J. P.; Burke, K.; Ernzerhof, M., Generalized Gradient Approximation Made Simple. *Phys. Rev. Lett.* **1996**, *77*, 3865-3868.

(8) Kresse, G.; Joubert, D., From Ultrasoft Pseudopotentials to the Projector Augmented-Wave Method. *Phy. Rev. B* **1999**, *59*, 1758-1775.

(9) Blöchl, P. E., Projector Augmented-Wave Method. *Phys. Rev. B* **1994**, *50*, 17953-17979.

(10) Monkhorst, H. J.; Pack, J. D., Special Points for Brillouin-Zone Integrations. *Phys. Rev. B* **1976**, *13*, 5188-5192.

(11) Krishna, R., Methodologies for Evaluation of Metal-Organic Frameworks in Separation Applications. *RSC Adv.* **2015**, *5*, 52269-52295.

(12) Krishna, R., Synergistic and Antisynergistic Intracrystalline Diffusional Influences on Mixture Separations in Fixed Bed Adsorbers. *Precis. Chem.* **2023**. https://doi.org/10.1021/prechem.2c00003.

(13) Yao, Z.; Zhang, Z.; Liu, L.; Li, Z.; Zhou, W.; Zhao, Y.; Han, Y.; Chen, B.; Krishna, R.; Xiang, S., Extraordinary Separation of Acetylene-Containing Mixtures with Microporous Metal-Organic Frameworks with Open O Donor Sites and Tunable Robustness through Control of the Helical Chain Secondary Building Units. *Chem. Eur. J*. **2016**, *22*, 5676-5683.

(14) Foo, M. L.; Matsuda, R.; Hijikata, Y.; Krishna, R.; Sato, H.; Horike, S.; Hori, A.; Duan, J.; Sato, Y.; Kubota, Y.; Takata, M.; Kitagawa, S., An Adsorbate Discriminatory Gate Effect in a Flexible Porous Coordination Polymer for Selective Adsorption of CO_2 over C_2H_2. *J. Am. Chem. Soc.* **2016**, *138*, 3022-3030.

(15) Yang, W.; Davies, A. J.; Lin, X.; Suyetin, M.; Matsuda, R.; Blake, A. J.; Wilson, C.; Lewis, W.; Parker, J. E.; Tang, C. C.; George, M. W.; Hubberstey, P.; Kitagawa, S.; Sakamoto, H.; Bichoutskaia, E.; Champness, N. R.; Yang, S.; Schröder, M., Selective CO_2 uptake and inverse CO_2/C_2H_2 selectivity in a dynamic bifunctional metal–organic framework. *Chem. Sci.* **2012**, *3*, 2993-2999.

(16) Chen, K.-J.; Scott, H. S.; Madden, D. G.; Pham, T.; Kumar, A.; Bajpai, A.; Lusi, M.; Forrest, K. A.; Space, B.; Perry IV, J. J.; Zaworotko, M. J., Benchmark C_2H_2/CO_2 and CO_2/C_2H_2 Separation by Two Closely Related Hybrid Ultramicroporous Materials. *Chem* **2016**, *1*, 753-765.

(17) Li, L.; Wang, J.; Zhang, Z.; Yang, Q.; Yang, Y.; Su, B.; Bao, Z.; Ren, Q., Inverse Adsorption Separation of CO_2/C_2H_2 Mixture in Cyclodextrin-Based Metal-Organic Frameworks. *ACS Appl. Mater. Interfaces* **2019**, *11*, 2543-2550.

(18) Qazvini, O. T.; Babarao, R.; Telfer, S. G., Selective Capture of Carbon Dioxide from Hydrocarbons using a Metal-Organic Framework. *Nat. Commun.* **2021**, *12*, 197.

(19) Xie, Y.; Cui, H.; Wu, H.; Lin, R.-B.; Zhou, W.; Chen, B., Electrostatically Driven Selective

Adsorption of Carbon Dioxide over Acetylene in an Ultramicroporous Material. *Angew. Chem. Int. Ed.* **2021**, *60*, 9604-9609.

(20) Gu, Y.; Zheng, J.-J.; Otake, K.-i.; Shivanna, M.; Sakaki, S.; Yoshino, H.; Ohba, M.; Kawaguchi, S.; Wang, Y.; Li, F.; Kitagawa, S., Host-Guest Interaction Modulation in Porous Coordination Polymers for Inverse Selective CO_2/C_2H_2 Separation. *Angew. Chem. Int. Ed.* **2021**, *60*, 11688-11694.

(21) Zhang, Z.; Peh, S. B.; Krishna, R.; Kang, C.; Chai, K.; Wang, Y.; Shi, D.; Zhao, D., Optimal Pore Chemistry in an Ultramicroporous Metal-Organic Framework for Benchmark Inverse CO_2/C_2H_2 Separation. *Angew. Chem. Int. Ed.* **2021**, *60*, 17198-17204.

(22) Shi, Y.; Xie, Y.; Cui, H.; Ye, Y.; Wu, H.; Zhou, W.; Arman, H.; Lin, R.-B.; Chen, B., Highly Selective Adsorption of Carbon Dioxide over Acetylene in an Ultramicroporous Metal-Organic Framework. *Adv. Mater.* **2021**, *33*, 2105880.

(23) Ma, D.; li, Z.; Zhu, J.; Zhou, Y.; Chen, L.; Mai, X.; Liufu, M.; Wu, Y.; Li, Y., Inverse and Highly Selective Separation of CO_2/C_2H_2 on a Thulium-Organic Framework. *J.Mater. Chem. A* **2020**, *8*, 11933-11937.

(24) Li, X.-Y.; Song, Y.; Zhang, C.-X.; Zhao, C.-X.; He, C., Inverse CO_2/C_2H_2 Separation in a Pillared-Layer Framework Featuring a Chlorine-Modified Channel by Quadrupole-Moment Sieving. *Sep. Purif. Technol.* **2021,** *279*, 119608.

(25) Cai, L.-Z.; Yao, Z.-Z.; Lin, S.-J.; Wang, M.-S.; Guo, G.-C., Photoinduced Electron-Transfer (PIET) Strategy for Selective Adsorption of CO_2 over C_2H_2 in a MOF. *Angew. Chem. Int. Ed.* **2021,** *60*, 18223-18230.

(26) Cui, J.; Qiu, Z.; Yang, L.; Zhang, Z.; Cui, X.; Xing, H., Kinetic-Sieving of Carbon Dioxide from Acetylene through a Novel Sulfonic Ultramicroporous Material. *Angew. Chem. Int. Ed.* **2022**, *61*, e202208756.

(27) He, C.; Zhang, P.; Wang, Y.; Zhang, Y.; Hu, T.; Li, L.; Li, J., Thermodynamic and Kinetic Synergetic Separation of CO_2/C_2H_2 in an Ultramicroporous Metal-Organic Framework. *Sep. Purif. Technol.* **2023**, *304*, 122318.

(28) Choi, D. S.; Kim, D. W.; Kang, D. W.; Kang, M.; Chae, Y. S.; Hong, C. S., Highly Selective CO_2 Separation from a CO_2/C_2H_2 Mixture using a Diamine-Appended Metal-Organic Framework. *J. Mater.*

Chem. A **2021**, *9*, 21424-21428.

(29) Zhang, Z.; Deng, Z.; Evans, H. A.; Mullangi, D.; Kang, C.; Peh. S. B.; Wang, Y.; Brown, C. M.; Wang, J.; Canepa, P.; Cheetham, A. K.; Zhao, D., Exclusive Recognition of CO_2 from Hydrocarbons by Aluminum Formate with Hydrogen-Confined Pore Cavities. *J. Am. Chem. Soc.* **2023**, https://doi.org/10.1021/jacs.3c01705.